Proc Indian Natn Sci Acad **80** No. 4 November 2014 (Special issue) pp. 827-876
© *Printed in India.*
DOI: 10.16943/ptinsa/2014/v80i4/55171

Review Article

High Energy Astroparticle Physics at Ooty and the GRAPES-3 Experiment

S K GUPTA
Tata Institute of Fundamental Research, Homi Bhabha Road, Mumbai 400 005, India

(Received on 06 December 2009; Accepted on 12 February 2014)

The astroparticle studies at Ooty have their roots going way back into the fifties, when studies using cosmic rays were initiated with cloud chambers of progressively larger sizes as the primary detector and measuring device to obtain properties of hadrons at high energies. This study was subsequently strengthened with the installation of a total absorption calorimeter and a modest extensive air shower array to probe the composition of the primary cosmic rays to very high energies. The discovery of pulsars provided a thrust for the exploration of these compact objects as the sources of γ-rays at TeV energies with the aid of atmospheric Cerenkov detectors in the seventies. With the rapid technological advances occurring during the subsequent years in detectors, electronics and computers, physicists world-wide were able to set up very large and remarkably sensitive experiments that were hard to imagine a decade earlier. With the increasing sophistication and complexity the modern experiments require participation of very large teams of scientists. This development has made the formation of collaboration of large number of physicists both experimental and theoretical, engineers, technicians etc., from a number of institutions and universities, a prerequisite for setting up any major experimental facility. The GRAPES-3 experiment is a collaboration of 34 scientists from 13 institutions, including 8 from India and 5 from Japan. The GRAPES-3 experiment contains a dense extensive air shower array operating with ~ 400 scintillator detectors and a 560 m^2 tracking muon detector (Em > 1 GeV), at Ooty in India. 25 % of scintillator detectors are instrumented with two fast photomultiplier tubes (PMTs) for extending the dynamic range to ~ $5x10^3$ particles m^{-2}. The scintillators, signal processing electronics and data recording systems were fabricated in-house to cut costs and optimize performance. The muon multiplicity distribution of the EAS is used to probe the composition of primary cosmic rays below the '*knee*', with an overlap with direct measurements. Search for multi-TeV γ-rays from point sources is done with the aid of the muon detector. A good angular resolution of 0.7^o at 30 TeV, is measured from shadow of the Moon on the isotropic flux of cosmic rays. Sensitive limit on the diffuse flux of 100 TeV γ-rays is placed by using muon detector to filter out the charged cosmic ray background. The tracking muon detector allows sensitive measurements on the coronal mass ejections and solar flares through Forbush decrease events. We have major expansion plans to enhance the sensitivity of the GRAPES-3 experiment in the areas listed above.

PACS: 13.85.Tp, 96.50.sb, 96.50.sd, 95.55.Vj, 98.70.Rz

Key Words: Cosmic Rays; Extensive Air Showers; Composition; Energy Spectra; Interactions; γ-Ray Sources

1. Introduction

The high altitude laboratory for cosmic ray studies at Ooty was set up in the premises of the Raj Bhavan in the mid-fifties, at the initiative of Dr. Homi J. Bhabha by one of his most illustrious associate, Prof. B.V. Sreekantan. It is a remarkable coincidence that the platinum jubilee of the Indian National Science Academy falls in 2009, a year that happens to coincide with two other epoch making events in the history of Indian science. As the year 2009 also marks the centenary of the birth of Dr. Bhabha and the

**Author for Correspondence: E-mail: gupta@grapes.tifr.res.in*

completion of 150 years of the birth of Acharya JC Bose. Acharya Bose had laid the foundation of advanced scientific research in India in the nineteenth century and Dr. Bhabha following in his footsteps nearly a half century later, created the edifice of modern scientific research in the country. In the present article we focus on a specific branch of research, namely, the area of high energy astroparticle physics where a unique facility, the Cosmic Ray Laboratory was created in the fifties which continues to expand and thrive till today.

1.1 Early History

During his inaugural address at the dedication of the Bose Institute in Kolkata in November 1917 Acharya J.C. Bose had stated, *But high success is not to be obtained without corresponding experimental exactitude, and this is needed to-day more than ever, and tomorrow yet more again. Hence the long battery of highly sensitive instruments and apparatus designed here, which stand before you in their cases in our entrance hall* [1]. This timeless statement remains as valid today as it did nearly a century back. That was also the spirit that drove Prof. Sreekantan and his colleagues in TIFR to develop a number of state-of-the-art instruments and detectors [2], starting with small to the world's largest cloud chamber for studying the interaction of hadrons in high energy interactions which lead to many interesting phenomena to be observed, including the first hint of rising hadronic interaction cross-section at TeV energies [3]. This result was soon verified by the then newly built colliding beam accelerator, ISR at CERN in Geneva, Switzerland.

The discovery of pulsars and their identification with rapidly rotating neutron stars with huge magnetic fields made them a natural candidate for the sources of high energy particles in the galaxy. This lead to a surge in world-wide experimental efforts to detect TeV γ-rays from these objects in the seventies. Employing the atmospheric Čerenkov technique, a major experimental initiative was launched at Ooty using a number of parabolic reflectors to search for γ-rays from pulsars, such as the ones in the CRAB and VELA supernova remnants. Rapid improvements in the sensitivity of these telescopes followed in the early eighties from the application of new techniques such as the optimization of aperture and fast timing of the Čerenkov shower front [4]. Subsequent development of the imaging technique achieved enhanced rejection of the charged particle background, completely transforming the field of γ-ray astronomy into a new window for the study of the universe. Clearly, new technological breakthroughs in the design of large reflectors and better data processing software have provided the launching pad for the developments and maturing of the atmospheric Èerenkov technique.

1.2 Energy Spectrum and Composition

The energy spectrum of the primary cosmic rays is remarkable, in that, it can be described by a simple power law over nearly 10 decades in energy, with only two significant changes in the exponent at ~ 3 x 10^{15} termed the *knee* and ~ 3x10^{18} eV termed the *ankle*. Despite a great deal of progress being made in recent times, a comprehensive understanding of the nature of the sources and the acceleration mechanism(s) responsible for the primary cosmic rays continues to elude us. In the absence of the direct detection of primary cosmic ray sources, owing to their deflection in the galactic magnetic field, precise measurements of the energy spectra of different nuclear components over a wide energy range could be helpful in deciphering the process of the acceleration of high energy cosmic rays and their propagation.

At energies ≤ 300 TeV, the direct measurements made by using the detectors flown aboard balloon and satellite borne platforms have provided crucial information on the composition and the energy spectra for various nuclear groups [5]. However, the results obtained from the direct measurements above 100 TeV suffer from limited statistics, due to the practical limitations on the size and weight of the space-borne detectors, which restricts the exposures to ≤ 10^3 m^2h. The indirect measurements on some of the components of an extensive air shower (EAS) such as the electrons, the muons, the hadrons, and the Čerenkov photons using the ground-based detectors, are the only available method for the study of the primary cosmic rays, wherein the exposure

factors of $>10^7$ m^2 h are achieved [6-11]. However, with the exception of the Tibet-ASg and ARGO-YBJ experiments [8, 9], the energy thresholds for most of the EAS arrays are significantly higher than the highest energy cosmic rays observed in the direct measurements. This is primarily due to the large atmospheric overburden at the observational sites, but also owing to the practical constraints, such as the large inter-detector separation in the shower arrays and the relatively smaller areas of the hadron and/or the muon detectors, that contribute to the higher threshold energies. Equally significantly, the results obtained from the observation of the EAS are strongly dependent on the details of the hadronic interaction generators used in the Monte Carlo simulations of the observed components of the EAS.

Due to the absence of the data from the accelerator experiments at $\geq$ 1000 TeV in the laboratory frame, especially in the *forward* region relevant for the propagation of the EAS in the atmosphere, the details of the assumptions made on the energy dependence of various interaction parameters, have a major impact on the final outcome. In the past, different characteristics of an EAS, such as the shower size (N_e), the electron-muon or the electron-hadron correlations, the Čerenkov photon density etc. have been exploited, for determining the nuclear composition and the energy spectrum at $\geq$ 1000 TeV. Unfortunately, the energy dependence of these components for different hadronic interaction generators are often significantly different. Therefore, it becomes necessary to validate a combination of these observables along with a hadronic interaction generator, by having an overlap with the results from the direct measurements. This objective has been rather difficult to achieve for most of the air shower experiments, due to a variety of practical reasons, some of which have been outlined above.

The GRAPES-3 observations of the muon multiplicity distributions (MMDs) [60, 61] for several shower size 'N_e' groups, have been used to obtain the energy spectra of various nuclear groups in the primary cosmic ray flux in the energy range ~ 100-1000 TeV. Therefore, a sizable overlap in the energy range ~ 100-300 TeV of the GRAPES-3 data with the direct measurements was achieved, that helped in the selection of a specific hadronic interaction generator as the preferred model, for the simulation of the EAS at energies ~ 100-1000 TeV. It is well-known that the correlation between the shower size N_e and the muon content N_μ is a sensitive probe of the composition of the primary cosmic rays.

The recent results from the Monte Carlo simulations have shown that the shape of the MMD measured with a large area muon detector possesses excellent sensitivity to the composition of the primary cosmic rays [10]. This is primarily because the lighter nuclei, such as the proton (H) and helium (He) etc. predominantly contribute to the lower multiplicity region of the MMD, as opposed to the heavier nuclei, namely, aluminum (Al) and iron (Fe) etc. that dominate the high multiplicity region. On the other hand, the medium nuclei such as the carbon, nitrogen and oxygen contribute to the mid-multiplicities in the MMDs. This fact may be readily understood, if one considers two primary cosmic rays, namely, a proton 'H' and an iron nucleus 'Fe', each having the same primary energy E_0. The Fe nuclei would break up in the very first interaction producing A nucleons each of which carrying an energy of ~E_0/A, where A is the mass number of Fe. Therefore, the subsequent hadronic interactions of these A nucleons would produce a larger number of charged pions of systematically lower energies than those produced in the interactions of H of the same primary energy. Therefore, the pions in the Fe initiated EAS would more likely decay, producing a significantly larger number of muons than in an H initiated EAS. These intuitive arguments are supported by the results of the detailed Monte Carlo simulations as would be shown subsequently.

1.3 Diffuse γ-Ray Flux ~ 100 TeV

The cosmic rays are the highest energy particles that are present in the nature with energies exceeding 10^{20} eV. The highest energy cosmic rays have been extensively studied over the past several decades, but their origin is yet to be clearly understood [12]. The current theories of the origin of the highest energy cosmic rays may be broadly classified into two distinct categories, namely, the "bottom up"

acceleration based models, and the "top-down" decay scenario. In the "bottom up"' scheme the charged particles are accelerated from low to high energies under very special astrophysical environments. Some of the examples of this approach include diffusive acceleration in supernova shocks, active galactic nuclei (AGNs), powerful radio galaxies, or the acceleration in the strong field associated with rotating neutron stars having high surface magnetic field. In contrast, the "top-down" invoke production of highest energy particles from the decay of sufficiently massive particles that had originated from the physical processes occurring in the early universe, thereby no acceleration mechanism is required [13].

The study of the highest energy cosmic radiation has been vigorously pursued, by using several large area extensive air shower (EAS) arrays with collection areas exceeding hundreds of km^2, to directly detect the extremely low fluxes of ≤ 1 km^{-2} sr^{-1} $century^{-1}$ expected of these particles [14, 15]. Recently, two new giant experiments, namely, the Pierre Auger Observatory (PAO) [16] and the Telescope Array (TA) [17] have been set up with effective collection areas in excess of 1000 km^2 for the study of the highest energy cosmic rays. Since the magnitude of the interstellar magnetic fields are insufficient to confine these particles to within the galaxy, the sources of highest energy particles are expected to be of extra-galactic in nature. The recent results from the PAO indicate that the hypothesis of a single power law beyond the *ankle* in the cosmic ray spectrum is not valid and their data are consistent with the existence of the so called Greisen-Zatsepin-Kuzmin (GZK) cutoff [18, 19] beyond the energy of 4×10^{19} eV [20]. An important corollary of this result is the large reduction in the flux of the highest energy cosmic rays. Therefore, the cosmic ray flux would be lower by more than a factor of ten at 10^{20} eV, as compared to the earlier estimates. Therefore, the number of events recorded, even by these giant experiments would be drastically reduced, thereby making the task of their study at the highest energies enormously more difficult.

However, there is a direct and intimate connection between the highest energy cosmic rays and the ultra-high energy (UHE, ~ 100 TeV) γ-rays. In principle, this connection may be exploited for an indirect study of the highest energy cosmic rays. Above the GZK cutoff around 4×10^{19} eV, the protons have a relatively short path-length before suffering photo-nuclear reactions with the photons of the 2.7^o K universal cosmic microwave background radiation, the relic of the big bang. The produced pions and other mesons decay into the electron, the photons and the neutrinos. Bethe-Heitler pair production in this photon field is also an important mechanism [21]. Since the electromagnetic decay products, namely, the photons and the electrons also have a relatively short path-length in the photon field of the cosmic microwave background radiation, electromagnetic showers develop in the universe as a consequence of the presence of the cosmic ray particles above the GZK cutoff. The observation of the UHE γ-rays that are the final outcome of the energy loss processes of the extremely high energy cosmic rays in the 2.7^o K background [22, 23] becomes an interesting probe of this mechanism. Extensive calculation have shown that the flux of 10-100 TeV γ-rays is within the reach of the planned γ-ray telescopes [24, 25].

Therefore, the presence of the UHE γ-ray component in the cosmic radiation offers an interesting possibility for further investigation. Specially, since it is possible to envisage the scenarios where the production of the cosmic rays is accompanied by the electromagnetic showers that might generate a sizable flux of the UHE γ-rays in the universe. The study of the γ radiation is of course extremely important in it its own right, because being neutral radiation, they are completely unaffected by the intervening interstellar and/or intergalactic magnetic fields and thereby retaining the sense of their original direction. Therefore, the γ-rays have the potential to provide significant information on the sites of the production and acceleration of the highest energy particles in universe.

There are a number of possible candidate sources for the production of the diffuse flux of UHE γ-rays. Some of the *conventional* scenarios for the production of these γ-rays include; (i) the unresolved point sources, such as the distant active galactic nuclei

(AGNs) and the powerful radio galaxies etc., which in addition may also be the sources of the extremely high energy cosmic rays, (ii) the decay of the mesons produced in the collisions of the charged cosmic rays with the interstellar and/or the intergalactic gas and dust, and finally (iii) the electromagnetic showers generated in the interactions of the extremely high energy cosmic rays with the cosmic microwave background photons.

In addition to the *conventional* sources, several *unconventional* astrophysical phenomena have been proposed that could produce a diffuse γ-ray flux at the UHE energies. For instance, it has been speculated that the highest energy cosmic rays may not be produced by any acceleration mechanism, but could be the decay product of some super-massive particles (generally termed the X particle) with mass $m_X > 10^{11}$ GeV that can have energies up to ~ m_X. Therefore, no acceleration mechanism is invoked to explain the highest energy particles. The massive X particles may have originated in the high energy processes in the early universe. Such an *unconventional* non-acceleration, "top-down" decay mechanism as opposed to the *conventional* "bottom-up" acceleration mechanism has significantly different predictions that may be experimentally verifiable [13].

In the top-down scenario of the origin of the extremely high energy cosmic rays, the X particles typically decay into quarks and leptons. The quarks undergo hadronization, producing jets of hadrons containing primarily light mesons with a small fraction of baryons. The pions decay into photons, electrons and neutrinos. Therefore, energetic photons, electrons and neutrinos together with a small percentage of nucleons are directly produced with energies going up to ~ m_X, without invoking any acceleration mechanism. For these decay products to be detected, either the X particles should decay in recent cosmological epoch, or the decay should occur at distances ≤ 100 Mpc from the Earth. The nature of the X particles is also a subject of considerable speculation. The X particles could be super-massive gauge bosons, Higgs bosons, super-heavy fermions produced from the collapse of the cosmic topological defects such as the cosmic strings, magnetic monopoles, superconducting cosmic strings etc., which may have formed in the symmetry breaking phase transitions associated with the grand unified theories in the early universe [26]. Te X particle could be a long-lived metastable super-massive relic of non-thermal origin, which may be produced through the vacuum fluctuations during a possible inflationary phase in the early universe. A fraction of such particles decaying in the recent epoch may give rise to the extremely high energy cosmic rays.

In the process of the collapse or the annihilation of the topological defects, the integral γ-ray flux at E ≤ 100 TeV is expected at the level of 10^{-3}-10^{-2} of the cosmic rays flux. These values were obtained by taking into account only the cascading in the field of the cosmic microwave background radiation. Due to the absence of definitive information about the level of the universal far infrared radiation, its role in the attenuation of the γ-ray flux is rather unclear. However, in the present discussion for the application of the SUSY GUT model, the far infrared radiation may also have a major impact on the observed γ-ray flux and its characteristic energy could come down by two or three orders of magnitude to ≤ 0.1TeV. Thus as a result, the diffuse γ-ray flux produced by the extragalactic cosmic rays would be drastically reduced and could become undetectable with the present generation of detectors.

As explained above, the highest energy charged cosmic rays during their passage through the intergalactic medium interact with the ubiquitous cosmic microwave background photons, resulting in the production of the pions including the π^0 s and other short-lived mesons. These interactions and decays occur repeatedly during the propagation of the cosmic rays over cosmological distances, resulting in a relatively rapid loss of primary energy leading to the occurrence of the so called Greisen-Zatsepin-Kuzmin or *GZK cutoff* in the primary cosmic ray energy spectrum at ~10^{20} eV [18, 19]. One of the end-products of these meson decays are the γ-rays, the electrons and the positrons. The interaction of this electromagnetic component in the photon field of the cosmic microwave background plays an important role through the following QED processes, namely,

(i) the pair production $\gamma\gamma \rightarrow e^+e^-$, (ii) the inverse Compton scattering of electrons $e\gamma \rightarrow \gamma e$, (iii) the electron pair production via virtual photons $e\gamma \rightarrow e^{+-}$ e, and finally (iv) the pair production $\gamma\gamma \rightarrow e^+e^-e^+e^-$. However, the two leading order processes, namely, (i) and (ii) dominate in the intermediate energy region between 10^{15} and 3x 10^{17} eV and above this energy domain the electron pair production via virtual photons dominates until the double pair production takes over above 7x 10^{20} eV.

As a result of the above mentioned processes, for distances of 100 Mpc or more become opaque to the propagation of the UHE γ-rays, and electrons due to the above mentioned interactions in the intergalactic medium. In summary, these interactions transfer the energy of the primary cosmic rays into the γ-rays of progressively lower energy and that in turn produce e^+, e^- pairs in the cosmic microwave background field, until the center of mass energy drops below the e^+, e^- pair production threshold. This occurs at ultra-high energies ($E\gamma \leq 100$ TeV). Thereafter the universe becomes relatively transparent to the propagation of the γ-rays of energy ~ 100 TeV. Thus a pileup of the γ-ray flux around ~ 100 TeV is expected. Since the sources of the highest energy cosmic rays are expected to be located at cosmological distances and therefore would be isotropically distributed. The resultant UHE γ-ray flux would constitute a diffuse and nearly isotropic background. Therefore, it is important to measure the flux of diffuse γ-rays at the UHE ($E\gamma \leq 100$ TeV) as a probe of the astrophysics of the cosmic rays at the highest energies [24, 25].

A measurement of the ratio of intensities of the diffuse γ- and cosmic rays in the energy region 20-500 TeV has therefore become of paramount importance. Some of the theoretical estimates show that at several tens of TeV, the diffuse γ-ray flux is enhanced as a result of the electromagnetic cascading from the interactions of the extremely high energy (~ 10^{20} eV) cosmic rays with the cosmic microwave background in the bottom-up [25], as well as, in the top-down models [27]. However, experimentally it is an extremely difficult proposition to distinguish the γ-ray from the charged cosmic ray induced showers with the ground based observations.

In the recent times have placed stringent upper limits on the diffuse flux of γ-rays which appear to question the validity of certain models in the several tens of TeV to a PeV (10^{15} eV) energy region. The HEGRA collaboration had used the HEGRA EAS array in association with the AIROBICC array of atmospheric Čerenkov detectors to probe the diffuse γ-ray flux in the energy region 65-200 TeV. They had placed a limit of 10^{-2} at 65 TeV on the ratio of the flux of γs to charged cosmic rays [28]. This upper limit at the time was a factor of 4 lower than the predicted ratio for one of the topological defect models [27]. In a subsequent report the HEGRA collaboration had reported an upper limit of 1.2 x 10^{-2} at 31 TeV and 1.4 x 10^{-2} at 53 TeV [29]. The EASTOP collaboration had also performed an extensive search for the diffuse flux of UHE γ-rays using the EAS with low muon content [30]. The CASA-MIA collaboration had reported sensitive upper limits on the diffuse flux of γ-rays in the energy range 500 TeV to 50 PeV [31].

1.4 Solar Flares, Coronal Mass Ejections

The solar flares and coronal mass ejections (CMEs) accelerate charged particles through a variety of mechanisms, which may be constrained through observations at high energies (> 10 GeV). The Sun is the closest astrophysical source accelerating particles to GeV and possibly higher energies, yet there is very limited understanding of, and little consensus on, the sites and processes leading to the production and acceleration of energetic particles associated with the solar flare activity [32, 33].

The available data obtained so far have shown that the solar flares and CMEs are a complex combination of a variety of physical processes involving the reconnection of the solar magnetic field lines due to certain instabilities occurring in the chromospheric and coronal regions surrounding the Sun. In some cases, the solar flares are observed in association with the CMEs. However, no such association between these two phenomena is seen in a number of other instances. The relationship between the emission mechanisms responsible for the solar flares and CMEs is an area of active research and much debate [34]. Solar flares are among the most

energetic events to occur in the solar system, releasing vast amounts of energy (~ 10^{25} J) on relatively short time-scales (~ 10^{2} s). The solar flares give rise to the emission of a variety of radiation ranging from radio, micro-wave, optical, soft and hard x rays and γ rays of up to several MeV including the γ ray lines due to nuclear de-excitation. Energetic solar particles contain electrons and ions which are accelerated in the solar flares [35].

Solar flares are classified into two broad categories, namely, "gradual" and "impulsive" flares. The gradual flares occur higher up in the corona and generally last for a longer duration of time and are also spread over a larger geographical region on the Sun. The gradual flares are also associated with CMEs and are accompanied with soft and hard x-ray emission. The ions accelerated in the gradual events display a composition which is rather similar to that of the coronal abundances. The impulsive flares on the other hand are believed to emanate from the regions closer to the Sun in the chromosphere and/or lower corona; the emission takes place for a shorter duration of time and over a relatively compact geographical region. The composition of the energetic ions in the impulsive events displays a very significant enhancement of the heavier nuclei as compared to the coronal abundances by an order of magnitude or more. In the case of helium, the ratio $^{3}He/^{4}He$, is observed to be ~ 1 as compared to the coronal value of ~ 10^{-3} [35-38].

Based on the observations, it appears that the ions in the gradual events are accelerated by a CME driven shock front. The shock front itself may be formed as a result of the magnetic reconnection, induced due to some instability in the coronal region. In the case of the impulsive events, several processes have been proposed for the modeling of the turbulent acceleration of particles in the flare region. Stochastic acceleration involving interaction of the particles with plasma waves gives a reasonable fit to some of the features of the energy spectra and the abundance ratios for several ions in the impulsive solar flares [35, 39-42]. However, some of the recent observations have shown that this canonical scenario of different acceleration mechanisms and characteristics for the impulsive and gradual flares is not always valid. It has been argued that the mechanism(s) responsible for impulsive events may also accelerate ions in some gradual events leading to a heavy ion rich impulsive composition in those cases [43]. Alternatively in some instances, shock acceleration could play a significant role in the acceleration of the particles in impulsive events. This hypothesis has been borne out by the observation of a CME in association with an impulsive flare on 1 May 2000 [44].

While the primary particles generated in a solar flare are charged, and are accelerated in the solar convection zones which serve to transfer energy to the interaction regions in the chromosphere, the γ-ray and neutron emission provides information on the interaction between solar energetic particles and the ambient medium around the Sun. For example, the temporal profiles of the γ-ray flux at different energies provide a wealth of data on the interaction of various particles and their entrapment near the Sun. The continuum γ-ray emission is produced due to the bremsstrahlung from high energy electrons. The bombardment of the chromosphere by high energy ions leads to the excitation of the ambient matter resulting in the emission of γ-ray lines in the MeV region due to the nuclear de-excitation in the chromosphere [45]. On the other hand, solar neutrons provide crucial information on the interaction of energetic ions, as the neutrons escaping into the interplanetary medium can be observed as decay protons or electrons by the detectors in space, and in rare cases, through the recoil protons in the ground-based NMs. However, the NMs mostly observe secondary neutrons produced by the interaction of primary protons with air nuclei.

In terms of the requirement for the energy budget, the conversion of the magnetic potential energy into other forms, during the process of magnetic reconnection [46, 47] provides a viable and attractive possibility to accelerate particles to several tens of GeV in a relatively short time. Therefore, there is a great deal of interest, in exploring the energy spectrum of the particles emitted during the solar flares, over a broad range of energy. This becomes especially important in view of the fact that the NMs

operating at high rigidities have only rarely recorded high energy events above 10 GeV. As in the other branches of astrophysics, a significant advance in the understanding of the phenomenon of the solar flares is unlikely to occur in the absence of multi-wavelength observations with a variety of ground- and space-based instruments. This approach has been successfully employed in the case of the large solar flare that had occurred on 29 September 1989 [45].

While the satellite-borne detectors with high sensitivity such as the instruments aboard the Advanced Composition Explorer [48] provide excellent measurements at sub-GeV energies, the energy range spanning from a few GeV to tens of GeV, can only be explored through the studies, with the network of NMs and muon telescopes located at various sites around the world. The highest energy of the particles accelerated during the solar flares is one of the decisive parameters that can be used to differentiate among various possible models of particle acceleration in the Sun. Observations of flare particles show spectra with cutoff at energies beyond a few GeV which have to be understood on the basis of the models of particle acceleration. Observations carried out using the detectors with high sensitivity opens up the possibility of search for particle fluxes at high energies near the cutoff and/or the shape of the energy spectrum near such cutoffs. Such measurements may provide new constraints on models of particle acceleration in solar flares. However, the galactic cosmic rays constitute the dominant background for the detection of the high energy (above tens of GeV) solar particles. The detection of the secondary muons (produced in the atmosphere by energetic solar particles) with the surface and the underground muon telescopes with good directional capability is an important tool to probe the high energy end point of the energetic solar particle spectrum. It has been pointed out that muon detectors with relatively good angular resolution may be able to observe the energetic solar particles at ~ 100 GeV.

In the past, there have been several reports of the detection of the bursts of muons which were nearly coincident in time with the associated solar flare activity in x rays, although with somewhat limited statistical significance [38]. One of the significant detection of a muon burst was by the Baksan group which occurred on 29 September 1989 at an energy of $\geq$ 200 GeV, indicating possible acceleration of the solar protons to several hundreds of GeV. However, the direction of this muon burst did not coincide with the direction of the Sun. Also the enhanced muon flux was observed after a delay of a couple of hours after the impulsive phase of the associated solar flare [49, 50]. The delayed arrival of the high energy solar particles opens up the possibility, in at least some of the solar flares, of the acceleration of high energy protons and ions after a significant delay, following the initial impulsive phase. The AGASA group had reported the detection of an enhanced flux of prompt muons during the solar flare of 4 June 1991, which they claimed was due to the arrival of the solar neutrons of energy $\geq$ 10 GeV [51]. The L3 group, using their precision tracking muon detectors at CERN, have reported the detection of a significant excess of muons in association with the solar flare of 14 July 2000 [52].

The occurrence of the solar flares and the CMEs result in a sudden injection of high energy plasma with frozen-in magnetic field lines into the interplanetary space. This phenomenon leads to the formation of a shock front in the interplanetary space surrounding the Sun. The electromagnetic field present in the plasma acts as a potential barrier for the incoming cosmic radiation, when the shock front passes in the vicinity of the Earth. As a consequence, the observed rate of the secondary particles (neutrons and muons etc. produced by the primary cosmic rays) in the atmosphere of the Earth registers a sudden drop, which is termed “Forbush decrease (Fd)” [53]. The passage of the Earth through the shock front results in the sudden commencement of a geomagnetic storm. Several variants of the shock models involving ordered and/or turbulent magnetic fields have been proposed to explain the phenomenon of Fd [54].

The Fds are characterized by a rapid decrease (~ 5-15 %) in the intensities of the observed muon and neutron fluxes at the Earth with an onset time, ranging from several hours to about a day. This is

followed by a relatively slower recovery time, ranging from about a week to several months. The magnitude of a Fd is defined as the fractional decrease in the intensity of the muon/neutron flux from its quiescent value. The magnitude of the Fds is observed to decrease with increasing rigidity. The Fds also display some correlation with the 11-year solar cycle. The occurrence of the Fds is generally accompanied by the observation of large anisotropies in the flux of the cosmic radiation [54]. The phenomenon responsible for a Fd evolves as it propagates farther into the heliosphere. This evolution results in a gradual increase in the onset and the recovery times with the heliocentric distance. There have been suggestions that the cosmic ray modulation with the 11-year solar cycle could be a result of the cumulative effects of the Fds occurring over a long period of time [55].

The ground-based NMs and space-borne detectors in general, have a very poor angular resolution. Therefore, the information on the directional dependence of the Fds is usually obtained from the worldwide network of ground-based NMs located all over the Earth, with the help of appropriate modeling techniques [56, 57]. However, due to the variation in the cutoff rigidity with the geomagnetic latitude of the site, various NMs respond differently to a given Fd event, thus making the interpretation of the observed data somewhat complicated and model dependent. However, a single monitor with a good angular resolution may be able to provide simultaneous information on the directional dependence of the observed Fd. In addition, the detectors located near the geomagnetic equator have rigidity cutoff, which varies rapidly with the arrival direction, thus permitting the measurement of the rigidity dependence of the detected Fd from a single instrument.

The search for the emission of protons of ≥ 20 GeV during the active phase of solar flares is an important activity using a large area tracking muon telescope of the GRAPES-3 experiment. Protons were accelerated during the solar flare on 28 October 2003 around 11:10 UTC nearly 80 min after the detection of this flare in the x rays. This solar flare had occurred in the active sunspot region 10486 in the east of the central meridian of the Sun. An intriguing feature of the solar flare of 28 October 2003 has been that the earliest arriving particles were recorded by the neutron monitors (NMs) viewing the anti-sunward direction. Also the enhancement in the nucleon flux continued for a long duration of time (~ 20 h) until the fast moving (mean velocity ~ 2200 km/s) coronal mass ejection (CME) shock front arrived at the Earth. Two distinct components, namely, a prompt and a delayed one, were observed by the global network of Earth-based NMs [58]. Detailed modeling of charged particle propagation in the interplanetary medium permeated with magnetic fields to explain, the delayed and the prompt components of the solar particles, observed by the worldwide network of a large number of NMs, has also been attempted. Here one exploits the delays in the onset of the rate increases seen in the NMs, to estimate that the path-length of the relativistic protons from the Sun to the Earth to be ~ 2.2 AU. This model implies that the acceleration of the protons in the flaring region is followed by their transport along a stretched magnetic field loop (~ 2.2 AU) to the Earth. During this period the Earth was located at the interface of the interplanetary CME and a co-rotating stream from the Sun. The direction of the loop from the anti-sunward direction was used to explain the direction of the radiation and the anisotropy seen in the NM data. The onset of the Fd started in the wake of the fast CME on 29 October 2003 nearly 20 h after the start of the X17 class solar flare at 09:51 UTC on 28 October 2003. Concurrent observations of sub-GeV solar neutrons using several NMs and of solar γ rays from INTEGRAL satellite have been made with good statistical significance. The correlation in the time profiles of the solar neutrons and the γ rays was used to conclude that the solar neutrons and the γ rays were produced at the same time [59].

The arrival of the CME on 29 October 2003, ~ 20 h after the start of the X17 class solar flare at 09:51 UTC on 28 October 2003, started the onset of a large Fd. New information on this Fd has been provided by the GRAPES-3 experiment. The magnitude of this Fd as measured by the GRAPES-3 experiment is ~ 8 % and a comparatively short onset

time of ~ 10 h and thereafter the recovery phase of the Fd commenced. The onset and recovery phases of this Fd display a rich time structure. The tracking feature of the muon telescope has shown a systematic time shift in the onset of the Fd on a time scale of an hour. By exploiting the tracking feature of the muon telescope for analyzing the rigidity of the incoming particles, the rigidity dependence of the magnitude of the Fd has been estimated [32].

With the passage of time it has been realized that measurement of as many components of the EAS as possible holds the key to the future success of these studies. The electrons, in an EAS are the most studied component for getting information on the shower, particularly for generating the trigger, determining the arrival direction and for estimating the energy of the primary particle. A measurement of the lateral (radial) density distribution of the particles in a shower using an array of unshielded charged particle detectors provides a good estimate of the observed number of particles in the shower. Despite considerable fluctuations in the development of individual showers in the atmosphere and the differences in the development profile for different primary nuclei, the shower size N_e is known to be a good parameter for estimating the primary energy of a shower. Practical and economic constraints limit the number of detectors deployed in a shower array, thus providing only a sampling of the particle density at a limited number of points. Even in good shower arrays, for example, the CASA-MIA [62], the Tibet AS γ [63] and the KASCADE [64] arrays, the detection area does not exceed about 1 percent of the physical area over which the array is spread out. However, this is an important parameter which contributes significantly to the accuracy of the measurement of shower size (and consequently primary energy) as well as the arrival direction, particularly for γ-ray astronomy. With similar considerations in mind, the GRAPES-3 EAS array has been designed to have one of the most compact configurations of conventional type arrays with only 8 m separation between adjacent detectors that are arranged in a symmetric hexagonal geometry. While the final target is to have 15 rings with 721 detectors, covering a distance of up to 120 m from the center of the array, the observations were started in early 2000 with 217 detectors located within the inner 8 rings which now have increased to 400 detectors. To extend the dynamic range of the primary energy it was decided to measure the density of the particles in the EAS with an enhanced range of up to 5000 m^{-2} [60].

Certain aspects of high energy cosmic ray astrophysics require correlated studies of the electron and the muon components of air showers, namely, the search for cosmic ray sources through γ-ray astronomy and studies of the variation of the nuclear composition of the primary cosmic rays with energy. While studies on the electron component provide basic information on the arrival direction and the energy, it is the muon component that plays a crucial role in distinguishing a primary γ-ray from a charged cosmic ray particle and in determining the composition. A large area (560 m^2), tracking muon detector of the GRAPES-3 experiment, operating at Ooty in southern India, was designed for the detailed studies on both of these aspects of cosmic ray astrophysics.

1.5 Role of Muons in Composition Studies

Observational studies during recent years have focused on two aspects of cosmic ray astrophysics, namely, the direct studies on the sources of γ-rays and the indirect studies on the nuclear composition of the cosmic rays. Although the importance of studies of TeV cosmic γ-rays for high energy cosmic ray astrophysics was highlighted in the fifties [66-68], the field of of TeV γ-ray astronomy advanced only in the eighties [69] following the breakthrough provided by the development of the imaging technique [70]. This was essentially due to an efficient rejection of the large background of charged cosmic rays. Similarly, at higher energies (10^{14}-10^{16} eV), another breakthrough has been sought by the use of the muon component [71, 72] for identifying the γ-initiated showers in the presence of a large flux of showers due to the charged cosmic rays. The Chicago Air Shower Array (CASA) in association with the Michigan Muon Array (MIA) was the first experiment to use an array of large area muon detectors to search [73] for muon-poor showers as a signal from potential γ-ray sources. The EAS-TOP [74], the KASCADE

[64, 65] and the GRAPES-2 [10] are the other recent experiments using either a large area muon detector or an array of muon detectors with the capability to observe the muon-poor showers. However, the GRAPES-3 experiment [61] with its single large area (560 m^2) muon detector is attempting to reach a significantly higher level of sensitivity to the γ-initiated showers based on their small muon content, particularly at the sub-PeV energies, lower than those achieved by the CASA-MIA experiment.

The muon component has been studied in recent experiments in two different ways. Using an array of muon detectors, the muon size is determined for individual showers from an integration over the lateral distribution function as fitted to the observed muon densities, for example in the CASA-MIA [62] and KASCADE [64] experiments. Using a single large area muon detector, such as in the EAS-TOP experiment [74], the muon size has been estimated for individual showers from the lateral distribution function obtained from a fit to the data. On the other hand, the GRAPES-2 [10] experiment had made a detailed study of the muon multiplicity distribution in an attempt to obtain the flux of the light nuclei (H+He+CNO groups) and the heavy nuclei (Si+Fe groups) in the cosmic rays almost independently. Pursuing the strategy of the GRAPES-2, the GRAPES-3 collaboration has constructed a large, 560 m^2 area, muon detector to study the muon multiplicity distribution for showers over a wide energy range.

1.6 Development of Cutting Edge Detectors and Electronics

With rapidly advances in the detector technology and specially in the area of signal processing and data recording it has now become feasible to set up large experimental facilities that were unthinkable even a decade back. As in other areas of science the progress in astroparticle physics is governed by the technological advances but with an additional requirement for a large number of instruments (channels). Therefore the development of the state-of-the-art equipment that is detectors and signal processing electronics is a key to the success in this field of research. Such an indigenous research and development activity offers numerous advantages from the point of view of cost and optimization according to the specific requirements of a given experiment. In addition, a home-grown capability allows rapid in-house repairs in the case of malfunctioning of the equipment, future improvements and continuous customization to suit the physics needs of the research activity. This is not something new but was the philosophy followed by Bose and Bhabha while laying the foundation of modern research in India as briefly mentioned at the start of this article. This was also the rationale for building a series of increasingly sophisticated cloud chambers to study the interactions of high energy hadrons in Ooty [2]. In the following we summarize some of the technological achievements that led to the development of high quality plastic scintillators.

The plastic scintillators are used extensively in the detection of charged particles in the experiments in the fields of nuclear physics, high energy physics, space physics and cosmic ray physics. In India high quality plastic scintillators are not available and have to be imported from abroad. High quality refers to a high light output (~ 50-60 % of anthracene) and good transmission of photons (attenuation length $\lambda \sim 50$ cm). The imported scintillators are prohibitively expensive and therefore involve large expenditure. Worldwide, only a handful of manufacturers, located in the USA, Europe and Japan supply plastic scintillators. In addition, sometimes there are certain complications in importing these scintillators. For setting up the GRAPES-3 experiment, in principle, our requirement could be met by importing plastic scintillators. But we decided against this easier but extremely expensive import option. For example, the high quality Bicron scintillator (BC-400 series) costs approximately Rs 100,000/- per m^2. Thus for 1000 m^2 of plastic scintillator for the GRAPES-3 experiment the import bill would have been substantial.

In the year 1998 an R&D program with the goal to develop high quality, low-cost plastic scintillators was started in Ooty. Since the bulk cost of styrene is low, we decided to purchase the basic raw material in the form of polystyrene granules. This was done to avoid the problem of inhibitors in liquid styrene.

Polystyrene granules were doped by the manufacturer with para-terphenyl and POPOP in specified quantities at the time polymerization as the primary and secondary scintillants. To the best of our knowledge no literature is available that describes the methodology for making high quality plastic scintillators from raw input. Since the casting of the high quality plastic scintillator in the form of sheets is a difficult process, any information pertaining to it, is kept confidential by the manufacturers. Therefore, we had to make a start from scratch. This R&D effort progressed steadily over the next 3 years in several distinct phases, successfully culminating in late 2001 with desired performance. The actual development is described in greater detail in a later section.

As already mentioned earlier the success of the experiment also critically depends upon the availability of high speed signal processing electronics. The photons produced due to passage of the charged particles through a scintillation detectors are converted into an electric pulse by the photo-multiplier tubes (PMTs). Intrinsically fast response (~ 1 ns) of a plastic scintillator can only be effectively utilized if the subsequent signal processing electronics has an equally short response time. The analog signals from PMTs have to be amplified and then converted into a digital signal by discriminators for subsequent use. A discriminator is operated at a user selected threshold and all signals with a pulse height below this threshold are rejected. Signals above the threshold trigger the discriminator and produce an output pulse of standard height and user defined width. Since there are no indigenous manufacturers of fast amplifiers and discriminators, therefore, every experimenter is forced to import these units from abroad. These units are very expensive and cost ~ Rs 5000 per channel. Since the requirement for the GRAPES-3 experiment is nearly 1000 channels, a goal was set to develop an 8-channel amplifier-discriminator module with a response comparable to the best imported modules.

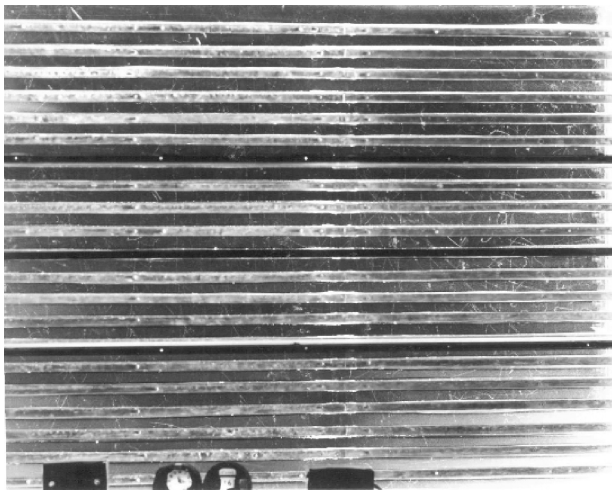

Fig. 1: A view of the high energy cascades developing in the largest cloud Chamber ever built

The direction of the shower is obtained from the accurate measurements of the arrival time of shower particles in the EAS array. The arrival times have to be measured to accuracies of ~ 1 ns. Multi-channel time to digital converters (TDCs) are used to perform this task to a precision of ~ 0.5 ns. In effect, the TDC is a fast stop-watch with sub-nanosecond accuracy and a large dynamic range with fast conversion time. Since there are no Indian manufacturers, the TDC modules have to be imported in large numbers at a very high price. However, a more serious constraint arises from the fact that in the case of a failure it takes a long time to get the imported equipment repaired. In the GRAPES-3 experiment where a large number of TDC modules are used the probability of a failure is not at all insignificant. Therefore, the development of high performance TDC had become a necessity for the success of this activity. Spread over a period of 5 years we had developed two models of the TDCs based on a application specific integrated circuit designed at CERN, Geneva called the TDC32 and HPTDC, respectively. The TDC32 based module contains 32 individual channels and it can measure a maximum time interval of up to 1 ms with a precision of 0.5 ns. The HPTDC based module with 32 channels can measure an interval up to 50 ms with 100 ps precision. In the subsequent discussion some of the salient features of these R&D activities are summarized.

2. The GRAPES-3 Experimental Setup

2.1 The Initial Array

The GRAPES-3 (Gamma Ray Astronomy at PeV EnergieS Phase-3) extensive air shower (EAS) array [60] has been designed to have one of the most compact configurations of the conventional type arrays with only 8 m separation between adjacent detectors that are arranged in a symmetric hexagonal geometry. The final target is to have 15 rings with 721 detectors, covering a distance up to 120 m from the center of the array, the observations were started in 2000 with 217 detectors located within the inner 8 rings. The GRAPES-3 experiment is located at Ooty (11.4°N latitude, 76.7°E longitude and 2200 m altitude), a popular mountain resort town in southern India. The GRAPES-3 EAS array shown in Fig. 2 at present time consists of 400 plastic scintillator detectors, each 1 m^2 in area. A schematic of the array is shown in Fig. 3, where each scintillator detector is represented by a filled triangle blue ▲ and the four muon supermodules are represented by filled squares green ■. Each filled square green ■ represents a 4-layer tracking muon detector with an energy threshold of 1 GeV along vertical direction. Each layer consists of 58 proportional counters (PRCs), each 6 m long with a 10 x 10 cm^2 cross-sectional area. This large area muon detector has been designed for the studies on the composition of the primary cosmic rays and studies on cosmic sources of multi-TeV γ-rays. Large area muon detector is also required for the observations on muons [32] produced by lower energy protons which are affected by the phenomena occurring on the Sun, such as the solar flares and the coronal mass ejections leading to magnetic disturbances around the Earth.

Each of the older shower detectors consists of four blocks of plastic scintillators, each 5 cm thick and 50 x 50 cm^2 in area, placed inside a square aluminum tank as shown in Fig. 4. A 5 cm diameter photomultiplier tube (ETL9807B) is mounted on top of a trapezoidal-shaped aluminum cone, with its face at a height of 60 cm above the scintillator surface. The inner surfaces of the tank and the cone have been painted with super-white (TiO_2) paint to increase the efficiency for collection of diffuse photons at the photomultiplier tube. The whole detector assembly is covered by a large aluminum cone to protect it from rain and heating due to direct sunlight. The detector is mounted on a 40 cm height stand, as shown in Fig. 4, to protect it from the flowing rain water. This arrangement allows a small muon telescope as shown in Fig. 4, to be placed under the detector for single particle (muon) calibration.

Fig. 2: GRAPES-3 Extensive Air Shower Array

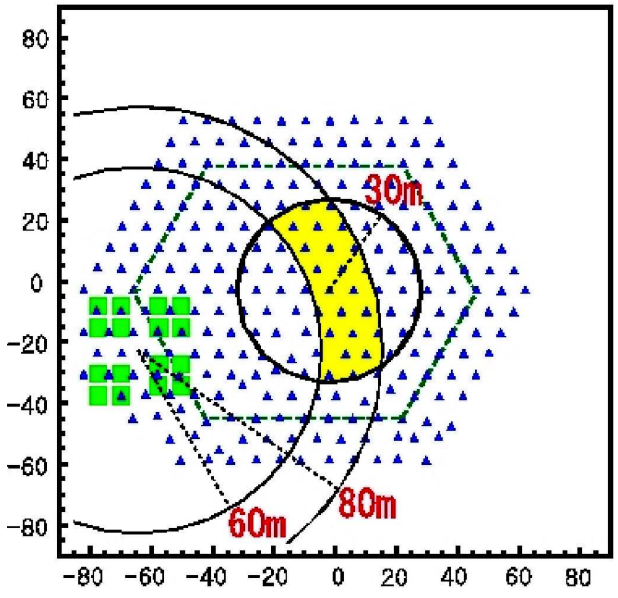

Fig. 3: The GRAPES-3 experimental system of 257 scintillator detectors (blue ▲) and 4 muon detector supermodules (green ■). Distances along X-, Y-axes are in meters

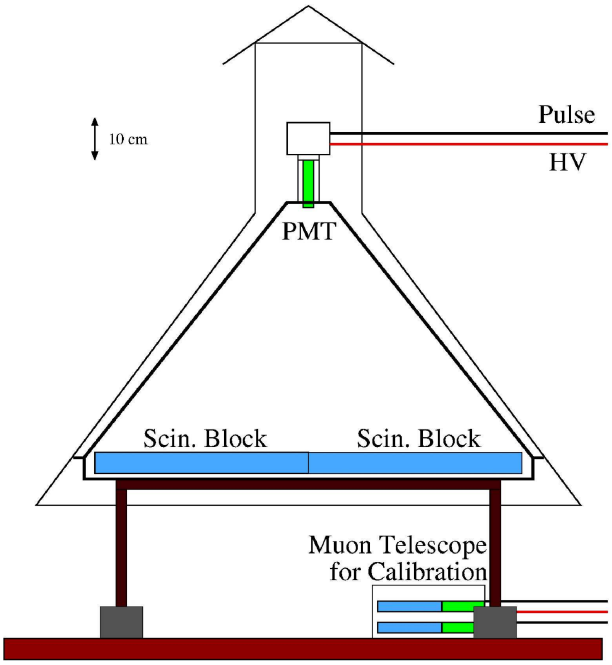

Fig. 4: Schematic of an old shower detector, including a muon telescope under detector for calibration

As shown in Fig. 4, the detectors are calibrated using a small muon telescope made of two (5 cm thick and 15x15 cm^2 area) independent scintillator pedals placed inside an aluminum box with a vertical separation of 5 cm between them. Each being fully sensitive to the passage of minimum ionizing particles, a 2-fold 100-ns coincidence between the two scintillators selects almost all muons with zenith angle $\theta \leq 50^o$. Most of these muons pass through the detector located above the muon telescope, thus providing the distribution of the integrated-charge for the passage of minimum ionizing particles. Typical single particle response for a detector in terms of the distribution of integrated-charge (ADC value) follows the Landau distribution [60]. The most probable ADC value obtained from the calibration distribution for each detector is used to convert the signal observed in a shower to 'equivalent' number of particles. The spatial non-uniformity in the response of the detector to single particles arises due to differences in the scintillation efficiency from block to block and due to geometrical effects. However, all the detectors have fairly uniform response, within ~ 10 %, over its surface of 1 m^2 area.

2.2 Development of High Quality Plastic Scintillators

Approximately 200 detectors could be deployed in the array by recycling the older scintillator blocks that became available following the closure of cosmic ray activity in the Kolar Gold Fields (KGF) near Bangalore. However, many of these scintillators were of poor quality and suffered from severe limitations such as low photon output and poor bulk transmission of photons and sizable non-uniformity. Unfortunately in the nineties due to low cost of imported styrene the indigenous manufacturers stopped its production completely and the group in BARC was forced to use imported styrene. Due to lack of large cold storage facilities within the country, imported styrene had to be stored at room temperature. Since styrene at room temperature undergoes gradual auto-polymerization the foreign manufacturers add so called 'inhibitors' to prevent the process of auto-polymerization. Unfortunately presence of these inhibitors kills the scintillating action of styrene based scintillators. Thus by mid-nineties the BARC had to abandon the production of scintillators. Therefore, by this time

there was no indigenous source of plastic scintillators in the country. The GRAPES-3 experiment was planned around this time with the aim of deploying an array of over 700 large (1 m^2) plastic scintillators. As mentioned above only partial requirement of the GRAPES-3 was met by recycling old scintillators which had became available after the closure of the KGF but we still needed another 500-700 m^2 of plastic scintillators. In principle, this requirement could be met by importing plastic scintillators. But we decided against this easier but extremely expensive import option. For example, high quality Bicron plastic scintillator (BC-400 series) costs approximately Rs 100,000/- per m^2.

In the year 1998 we started an R&D program with the goal of making high quality, low cost plastic scintillators. Since the bulk cost of styrene is low we decided to purchase the basic raw material in the form of polystyrene granules. This was done to avoid the problem of 'inhibitors' in liquid styrene. Polystyrene granules were doped by the manufacturer with 1 % para-terphenyl (primary scintillator) and 0.03 % POPOP (wave-length shifter) as specified by us at the time of polymerization. The granules by weight are approximately a factor of 15-20 lower in cost as compared to the finished scintillator. To the best of our knowledge no literature is available that describes the methodology for making high quality plastic scintillators. Since the casting of high quality plastic scintillator in the form of sheets is a difficult process, any information pertaining to it, is kept confidential by the manufacturers. Therefore we had to make a start from the very beginning. This R&D effort progressed over the next 3 years in several distinct phases before successfully culminating in world-class scintillator in late 2001. The performance of the scintillator may be summarized as follows, it has a decay time of 1.6 ns with a photon output which is 54 % of anthracene and an attenuation length ~ 100 cm. These parameters are comparable to the best quality scintillators available world-wide at a fraction of their cost. In addition, we have the unique advantage that we could manufacture scintillator of any shape and size exactly according to our requirements. Since all high quality plastic scintillators depend on total internal reflection for efficient collection of photons, all scintillator surfaces are required to be in highly polished state. Commercial scintillators are normally delivered with two surfaces in polished state but not the four edges. Polishing of the scintillator is technically a very challenging and expensive proposition. Cost of polishing of the scintillator edges can be comparable to that of scintillator itself. We have also developed the necessary technique to produce scintillators with polished edges. The development of scintillator in the Cosmic Ray Laboratory at Ooty has provided a major impetus to the GRAPES-3 experiment by providing high quality, customized plastic scintillator at a low cost. Taking advantage of this development we have also designed new state-of-the-art plastic scintillator detectors for the expansion of the GRAPES-3 experiment which are vastly superior to the earlier detectors that are described below.

2.3 New High Performance Scintillator Detectors

In view of the difficulties outlined earlier it was decided that for further expansion of the array, an alternative readout of the scintillator using wave-length shifting (WLS) fibers would be employed in association with the newly developed plastic scintillators. This resulted in an improved performance with a larger photon signal and a more uniform response. With the inclusion of a second PMT, the dynamic range for particle detection was increased to ~ 5 x 10^3 particles m^{-2}. The use of the plastic scintillators, developed in-house to cut costs thus also resulted in a vastly improved performance [75]. An efficient detector system should provide a large separation between the PMT noise and the signal due to the charged particles in the EAS, and should also have a uniform spatial response over the entire area of the scintillator. As already mentioned earlier that in the original GRAPES-3 trapezoidal shaped detectors, the scintillation photons collected at the PMT are, primarily due to diffuse reflection from the inner walls of the container [60]. This is not an efficient process, and results in a sizable loss of the signal. Most of the scintillator detectors had a photon output $\leq$ 10 photo-electrons, even for the 5 cm thick scintillators used. The geometry of the detector also resulted in a large spatial non-uniformity in the signal

across the detector and a variation ~ 30 % was observed in photon output from the center to the edge of the detector. In view of these limitations, we had investigated the use of wave-length shifting (WLS) fibers for an efficient collection of photons.

Observation of the photon pulses with a decay time of a few nanoseconds in plastic fibers were reported in 1981 and subsequently, extensive development of the plastic fibers occurred. Use of WLS fibers, where wave-length shifting cores ranging from several hundred microns to a few mm diameter, surrounded by single or multiple layers of cladding of progressively lower refractive indices were developed. The double-clad WLS fibers provide readout of the blue photon emitting scintillators in a detector, with the subsequent re-emission of the photons in the green wavelength using a 3-hydroxyflavone (3HF) type wavelength shifter present in the core material. A fraction of the re-emitted photons are transported to the end of the fiber through total internal reflections. It is known that the double clad fibers provide an improved photon yield of up to 70 % higher than the single clad ones, by increasing the fraction of light trapped through total internal reflections [75].

A new scintillator detector has been developed with significantly improved performance, by suitable placement of the WLS fibers in machined grooves on the scintillator surface. Since, the spatial uniformity and the response time of the scintillator critically depends on the layout of the fibers, the performance of the detector was also simulated using a Monte Carlo simulation code 'G3ScSIM' developed by us for this purpose. A direct comparison of the results from the simulations and the actual measurements allowed, a better understanding of the performance of the detector to emerge. Three different layouts of WLS fibers were evaluated using Monte Carlo code, G3ScSIM. However, the final configuration was adopted on the basis of cost effective fabrication with excellent uniformity and high photon output. The saturation of the PMTs encountered at very high particle densities in the earlier GRAPES-3 detectors, limited their use over a wider range of primary cosmic ray energies. To overcome this limitation, the WLS fiber detectors were designed with two PMTs.

In the present study, Kuraray double clad WLS fibers of type Y11 (200) were used. These 1 mm diameter fibers consist of a central polystyrene core (refractive index $\eta = 1.59$) with two outer claddings of progressively lower refractive indices. The inner cladding is polymethyl-methacrylate (PMMA) with $\eta = 1.49$ and the outer cladding is fluorinated polymer (FP) having $\eta = 1.42$. All fibers are cut to a length of 1.3 m. To place the WLS fibers inside the scintillator, 1.5 mm wide and 2 mm deep grooves have been machined on the surface of the scintillator (50 cm x 50 cm^2 cm). Three different groove designs named, 'parallel', 'matrix' and 'σ' were investigated. The layout of these 3 designs are schematically shown in Fig. 5. Since the *parallel* and *matrix* grooves are straight, they are machined using an ordinary milling machine. However, the σ grooves require the use of a CNC milling machine.

For the *parallel* and the *matrix* configurations, a total of 12 grooves with equal inter-groove separation were machined. An inter-groove separation of 4.0 cm was used for the *parallel* grooves (50 cm long) as shown in Fig. 5a. For the *matrix* grooves the separation was 9.6 cm, for the two mutually orthogonal sets of 6 grooves (50 cm long), as shown in Fig. 5b. A total of 16 σ grooves were machined, each 41 cm long as seen in Fig. 5c. The total length of the WLS fibers embedded in the scintillator was 900 cm in the cases of the *parallel* and the *matrix* groove configurations. The WLS fibers are restrained from any movement by applying tiny strips of adhesive aluminum tape just above the groove. A total of 18 fibers used were placed in alternative grooves as single and two fibers, respectively. The total length of WLS fibers was 656 cm for the σ configuration with only one fiber in each groove as shown in Fig. 5. The entire scintillator and WLS fiber assembly was wrapped inside two layers of Tyvek paper, which acts as an efficient but diffuse reflector, resulting in a substantial enhancement in the number of the photons collected. Tyvek was chosen for its high reflectivity, chemically inert nature and excellent mechanical strength. Since only a small fraction of

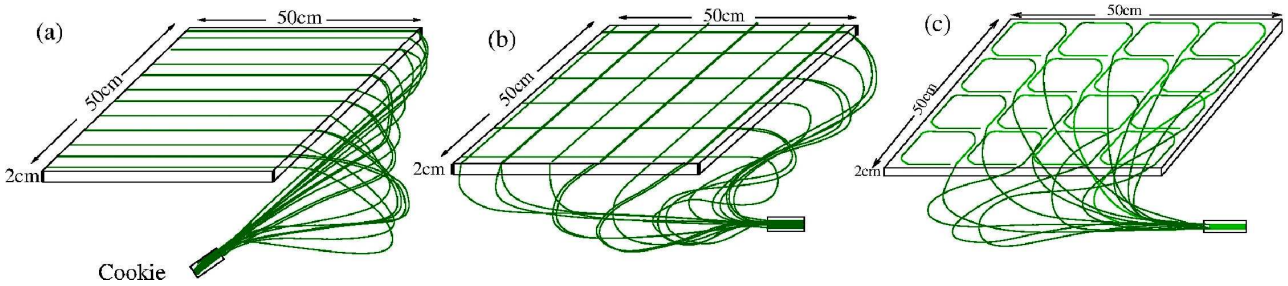

Fig. 5: The three groove layouts on the scintillator surface with embedded WLS fibers, (a) *parallel*, (b) *matrix*, and (c) σ

the total length (41 or 50 cm) of WLS fiber is embedded inside the groove, the remainder was used for its smooth and safe bending, en-route to the PMT. The free ends of the WLS fibers were bunched together and glued into an acrylic disk called a 'cookie' which was finally coupled to the PMT using an optical glue. The entire assembly was placed inside a light-tight aluminum tank. The experimental conditions were kept unchanged during the tests with different groove designs.

Prior to the actual experimental measurements, a Monte Carlo simulation code 'G3ScSIM' [75] was developed to obtain an understanding of the response of the scintillator for different fiber configurations. The G3ScSIM is basically a photon tracking code, for a plastic scintillator of rectangular geometry, with embedded WLS fibers of cylindrical geometry. In this code, the trigger conditions were kept identical to the one in the experiment with cosmic ray muons. The important input parameters used in G3ScSIM are summarized in Table 1. Some of the simplified assumptions made in G3ScSIM were; (i) the scintillator response is homogeneous, (ii) the scintillator photons are monochromatic, and (iii) the WLS fibers are in optical contact with the scintillator surface, over an area projected by it. A brief description of some of the relevant features of G3ScSIM code are summarized below.

The cosmic ray muons were simulated over the surface of the scintillator with random coordinates x, y and arrival direction; zenith angle θ ($0 \leq \theta \leq 60^{o}$), azimuthal angle ϕ ($0 \leq \phi \leq 360^{o}$). A trigger was generated, only if a muon passes through all the five triggering detectors. The energy loss - dE/dx of the

Table 1: Monte Carlo simulation parameters

Scint. Refractive index (η_{sc})		1.59
WLS (η_{wls})	core	1.59
	in .clad	1.49
	out. clad	1.42
Scint. decay time		1.7 ns
WLS fiber decay time		6.1 ns
Scint. attenuation length		100 cm
WLS attenuation length		350 cm
Tyvek reflectivity		90 %
ETIR		93 %
PMT time jitter (FWHM)		2.2 ns
Mean energy loss/photon		100 eV

muon, in the scintillator was calculated using the Landau distribution based on an algorithm from the CERN library. A production rate of one short wavelength (blue) photon per 100 eV energy loss was assumed. The blue photons were generated along the track of the muon, every 0.1 mm, with the emission angles θ and ϕ, selected randomly from an isotropic angular distribution. The emission time of each photon was calculated from an exponential distribution with a decay time of 1.7 ns for the scintillator, as was measured by us earlier.

The propagation of the blue photons in the scintillator was tracked, by a ray tracing method, governed by the laws of geometrical optics. The incidence of a photon on the scintillator surface was determined, from among the six surfaces of the

scintillator. At every reflection from the scintillator surface, three possibilities exist, namely; (i) the absorption of the photon in the scintillator, (ii) the interception by a WLS fiber, and (iii) the reflection from the scintillator surface. To determine absorption of a photon in the scintillator, the total path-length traversed was compared with the survival path-length for that photon, using the Monte Carlo technique. Normally a photon incident on the scintillator surface at an angle greater than the critical angle, would undergo total internal reflection from a flat surface. However, the scintillator surface is not perfectly flat and any departure from the flatness would result in the escape of the photon. This effect was taken into account by assuming an effective total internal reflectivity (ETIR) < 100 %. The exact value of ETIR was determined empirically as described below. The Tyvek wrapping of the scintillator provides an efficient and diffuse reflecting surface of known reflectivity, for the photons escaping from the scintillator back into the scintillator. The photon reflection probability from the diffuse reflector was calculated using the Lambert's cosine law, where the angle of reflection is independent of the incident angle. However, when the scintillator was wrapped inside a black plastic sheet, the reflectivity from its surface of escaped photons was assumed to be zero.

To determine the incidence of a photon on the WLS fiber, we assumed the area projected by the fiber on the scintillator surface as the overlap area. A photon incident on the overlap area was deemed to have been absorbed by the fiber. Subsequently, a new longer wave-length (green) photon was generated with a wave-length distribution derived from the emission spectrum of WLS fiber, and tracked in case of trapping in the fiber, using the critical angle condition. At this point, a new start time was generated from the measured decay time (6.1 ns) of the WLS fiber. This in turn was added to the earlier transit time of the blue photon, from the time it was generated in the scintillator to the time of its absorption in the fiber. A trapped green photon was propagated, until it was absorbed in the fiber due to attenuation or if it reached the collection end of the fiber. The green photons propagating in the direction opposite to that of the PMT were assumed to be lost. The green photons reaching the PMT were converted into photo-electrons at the photo-cathode using the wave-length dependent quantum efficiency of the PMT. The amplitude and the response time of the PMT were convoluted to generate the PMT pulse. For each muon, the recorded information includes the X, Y coordinates, also the photon statistics such as the number of photons (i) produced in the scintillator, (ii) escaped from the scintillator, (iii) lost due to the attenuation, (iv) absorbed in the WLS fiber, (v) escaped from the fiber, and finally the number of the photo-electrons and their arrival times at the PMT.

A Monte Carlo simulation can reproduce the experimental data only if the detector parameters describing its performance are sufficiently close to their true values. These parameters include the scintillation efficiency, the surface reflectivity, the attenuation length, and the decay times etc. Many of these parameters were directly measured by us or were available in the literature. The remaining parameters had to be obtained by assuming some initial values and then fine tuning those values by matching the simulation results with the experimental data for a particular configuration of the detector. The results could then be cross checked by carrying out another set of measurements with a different configuration of the detector. To fix the free parameters in the simulations, the *parallel* groove design, with and without the Tyvek wrapping was modeled. The only free parameter used in these simulations was the ETIR. The initial value of the ETIR was taken to be 100 %, implying that the scintillator surfaces to be perfectly flat. The resultant photon distribution from the simulations disagreed with the experimental data. It was observed that the simulated ratio of the mean number of photons with and without the Tyvek wrapping was 2.2, while the experimental value was 3.3. It was observed that this ratio increases with decreasing value of ETIR. A value of ETIR = 93 %, gave a nearly perfect agreement with the experimental data. This value of the ETIR was used for all subsequent simulations.

The muons suffer a mean energy loss of 1.89 MeV/cm in a scintillator. However, when due account was taken of the muons arriving from different

directions that trigger the setup, the mean energy loss becomes 4.6 MeV in the 2 cm thick scintillator used. This results in the production of a large number of photons (~ 46000), but only a small fraction eventually reaches the PMT. The simulations showed that ~ 86 % of the produced (blue) photons were either absorbed or escaped from the scintillator. The mean path-length traversed by the blue photons was ~ 51 cm and the mean number of reflections was ~14 inside the scintillator. Therefore, ~14 % of blue photons managed to enter the WLS fiber, which after initial absorption were re-emitted as green photons. Furthermore, because of the large value of the critical angle, most of the green photons escaped from the WLS fibers, and only ~14 % of the photons were trapped. These photons travelled along both directions in the fiber. The mean path-length traversed by the green photons was ~ 112 cm and the mean number of reflections was ~ 430 prior to reaching the PMT. Finally, only ~ 0.45 % of the total photons produced in the scintillator, namely ~ 208 photons arrived at the PMT.

The main design objective for the new detector was to efficiently record the shower particles over a large dynamic range (1-10000 particles), to cover a wide range in the energy spectrum of the primary cosmic rays from ~ 10^{13}, where the particle density at the core is rather small; to ~10^{17} eV where densities may reach several thousand particles m^{-2}. Efficient detection of a single or a few particles was ensured by designing a detector with high photon yield and good spatial uniformity. The high photon yield also implies that the PMT could be operated at a relatively lower voltage, thereby reducing the noise and increasing its life. The PMTs are typically operated at gains of (3-5) x 10^6. However, at high particle densities, the anode current become very large and the PMT response become non-linear. For the ETL-9807B PMT used here, the response became non-linear at a peak anode current of 50 mA to 150 mA. This translates into the onset of the non-linearity at ≥ 50 particles and of saturation at ~ 100-200 particles. This introduced error in the estimation of the various shower parameters. Although, one could use the signal from an earlier stage of the dynode chain to avoid saturation, we preferred to employ a second PMT to enhance the dynamic range of our detectors.

As described below, through a study of the; (i) photon output, (ii) uniformity and (iii) the time response for different groove designs, we found that the simple and inexpensive *parallel* groove configuration met our design goals. Using four scintillator tiles, a 1 m^2 detector was fabricated. The side-view of a complete dual-PMT WLS fiber detector is shown in Fig. 6. The single-PMT fiber detector was identical to a dual-PMT detector, except that it was operated with only one high-gain PMT. The photons from each 50 cm x 50 cm scintillator tile were collected by 18 fibers for the high-gain PMT, whereas only 6 fibers were used for the low-gain PMT. The groups of 18 and 6 fibers for the high- and low-gain PMTs were placed inside 12 grooves, as has been described earlier. Two groups of fibers from the four scintillators are coupled to two PMTs,

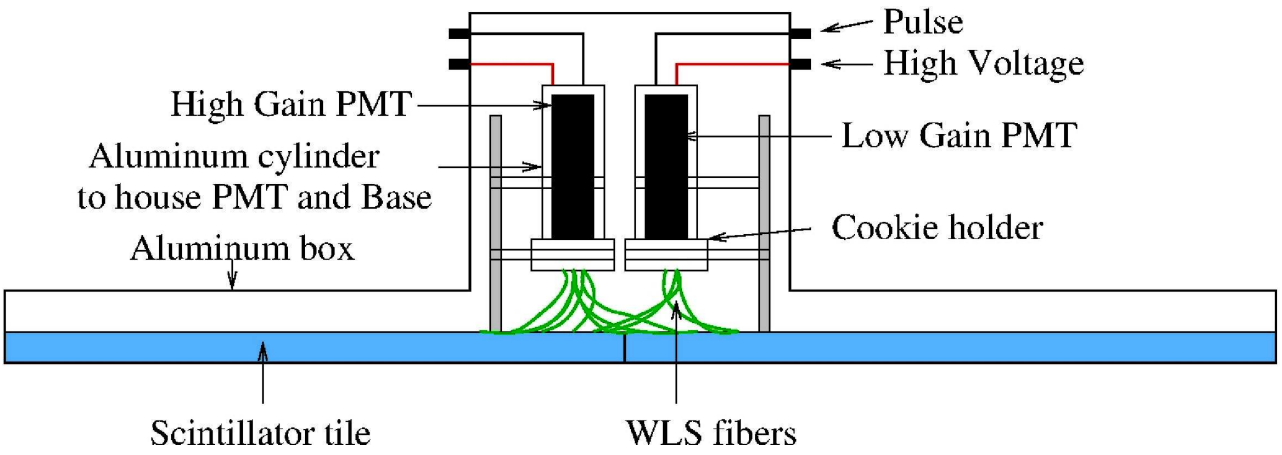

Fig. 6: Side view of a dual-PMT fiber detector. Total number of fibers from the scintillator to high-gain PMT was 72 and to low-gain PMT 24

through two separate cookies; the first containing 18 x 4 = 72 fibers to the high-gain PMT, and the second 6 x 4 = 24 fibers to the low-gain PMT.

A comparison of the photo-electron distributions for the *parallel*, the *matrix*, and the σ groove designs for the experimental data and the Monte Carlo simulations are presented in Fig. 7, and the results are also summarized in Table 2. Here it needs to be emphasized that the simulation parameter 'ETIR' was extracted, using only the *parallel* groove data and then subsequently used for the *matrix* and the σ grooves. An excellent agreement between the photo-electron distributions from the data with the Monte Carlo simulations for the remaining two designs, namely, the *matrix* and the σ is seen in Fig. 7. Further, it may be seen from Table 2 that the photo-electron yield in the case of the *parallel* groove is comparable to that of the *matrix* groove, whereas it was significantly lower in the case of the σ groove. The embedded length of the fibers in the σ groove was 27 % less, as compared to the other two groove designs, however, the photo-electron yield in the σ groove was 13 % less as compared to the *parallel* groove and 18 % less compared to the *matrix* groove. Thus the photo-electron yields per unit length of the embedded fiber, for the three groove designs were comparable to within ~10 %, irrespective of the shape and the layout of the grooves. Based on these results, it was decided to employ the *parallel* groove configuration, since it is economical to implement and the assembly of the detector is also relatively simpler.

The variation in the response, across the scintillator surface for all the three groove designs with Tyvek wrapping, were carefully studied. In the case of the *parallel* groove, a small decrease in the photon output was observed, from near the PMT end to the far end of the fiber. In the *matrix* groove, a similar trend with reduced magnitude was seen. However, in the case of the σ groove, no such variation was observed. Also no transverse variation in the photon output was observed for the *matrix* and σ grooves, whereas for the *parallel* groove the edge response was slightly higher than from the central area as stated above. The root mean square (rms) non-

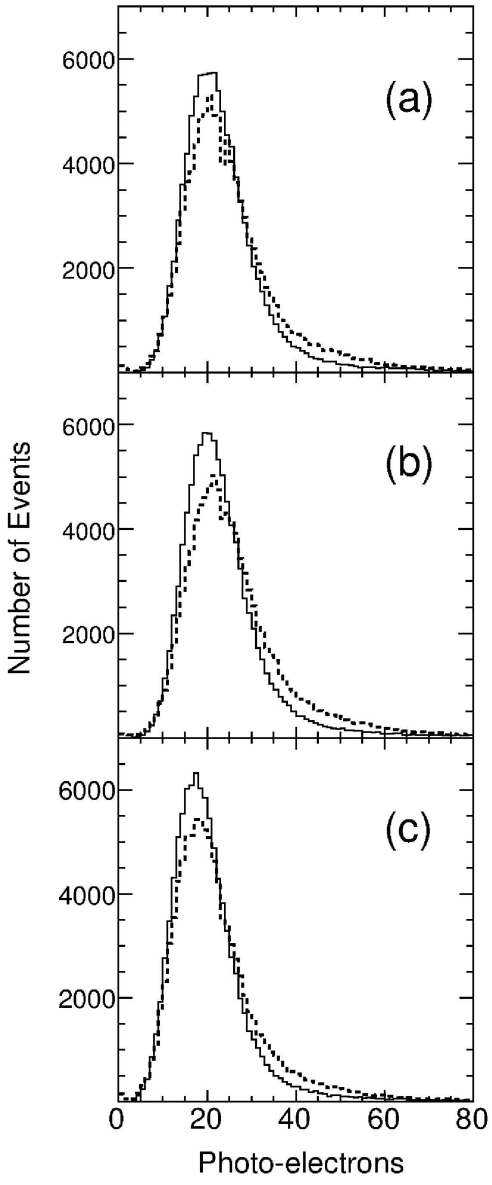

Fig. 7: Photo-electron distributions; (a) *parallel* groove, (b) *matrix* groove, and (c) σ groove. Experimental data shown by dashed line and Monte-Carlo results by continuous line

Table 2: Photo-electron yield of scintillator for different WLS fiber configurations

Groove	Fiber-length	Photo-electrons
Parallel	900 cm	20.5
Matrix	900 cm	21.7
σ	656 cm	17.9

uniformity for the three groove designs was calculated separately, for both the data and simulations and these results are summarized in Table 3. The simulated

Table 3: Uniformity in different groove patterns

Groove type	RMS non-uniformity (%)	
	Experiment	Monte Carlo
Parallel	2.7	2.0
Matrix	2.1	1.6
σ	3.5	3.3

values of the rms non-uniformity was always slightly smaller (0.2-0.7) %, than the corresponding experimentally measured value for all three designs. This was not surprising, in view of the fact that many of the simplifying assumptions in the simulations only provide approximations to the real world. For example, any imperfections on the surface of the scintillator or any variations in its density, would result in an enhanced rms non-uniformity in the experimental data. However, the rms non-uniformity was less than 4 % for all three groove designs, well below the acceptable level of 5 %.

2.4 The GRAPES-3 Trigger

The symmetric hexagonal geometry, used in the deployment of the detectors was employed, to ensure a uniform selection of the showers, over a well-defined area of the array as shown in Fig. 3. The array also contains a large (560 m^2) tracking muon detector in the form of four supermodules, that are visible as the four large halls in the top-center region of Fig. 2 [61]. These halls also house the signal processing and recording electronics for the muons, for that supermodule. Each 140 m^2 area supermodule, in turn comprises of four modules. The muon detectors provide a reliable estimate of the muon multiplicity, even for a low energy EAS.

The anode pulse from each shower detector is taken to the central control room using a 230 m long co-axial cable. It is then passively split into two pulses, one a.c. coupling to a channel of the CAEN (Model C205N) 32-channel, 15-bit dynamic range, ADC module through some additional cable delay (80 m co-axial cable). The second pulse is amplified by a factor of 10 before being fed to the discriminator set at a threshold of –30 mV. One of the outputs of the discriminator goes to a channel of the TDC (200 ps resolution) while the other output goes for shower selection as well as to the rate monitoring system. In order to achieve a low energy threshold for the trigger, a simple 3-line coincidence was used to generate the Level-0 trigger, as shown in Fig. 8, which acts as the GATE for the ADCs and START for the TDCs. Looking at the detectors lined up in the North-South direction, the signals from the discriminators for all the detectors in a given line are OR'ed together. Then a 100 ns wide, 3-fold coincidence is generated among the line OR's for each combination of three adjacent lines. All these 3-line coincidences, (L1.L2.L3), (L2.L3.L4), (L3.L4.L5), etc., are OR'ed together to generate the Level-0 trigger. Note that only the inner 6 rings (detectors 001 to 127) of the 8 rings were used for generating the line OR's in order to optimize the selection of showers with cores incident within the array. The observed level-0 trigger rate currently is 70 Hz. Not surprisingly, this trigger selects a sizable number of small but local showers and also very large

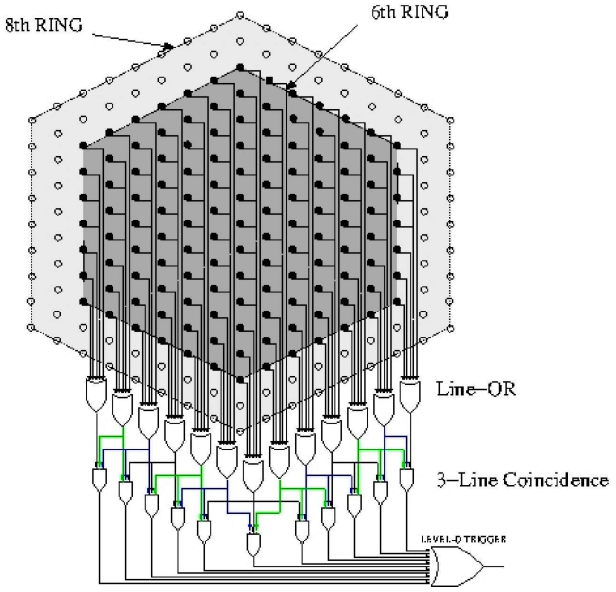

Fig. 8: Schematic of the shower trigger system for generating the Level-0 trigger using the basic 3-line coincidence from among the inner 127 detectors (6 rings)

showers whose cores located far away from the array. Therefore, an additional condition was imposed on the shower selection, namely, a requirement that at least 'n' out of 127 detectors should have triggered the discriminators within 1 ms using relatively slow EPROMS [60]. The observed shower rate for this Level-1 trigger currently is ~ 30 Hz for a value of n = 10 used in the experiment.

2.5 Rate Monitoring

The stability of the response of the shower detectors is an important parameter to ensure the stability of the trigger energy threshold. While single particle calibrations, as discussed above are carried out about once in a month, the counting rate for each detector is recorded for every 100 ms using the output pulse from the discriminator through the 'RATE MONITOR' system designed for this purpose. This is an independent data recording system which was designed to look for short term transients and correlations of the detector rates with atmospheric parameters.

In Fig. 9 variation in the rates for three of the 217 detectors namely detector numbers 06, 16 and 30 over a period of seven days during 15-22 February 2001 along with the variations in the shower trigger rate (Level-1), the atmospheric pressure and the temperature are shown. As expected the temperature shows diurnal variation in phase with solar radiation received on ground as seen in Fig. 9f. However the pressure data as seen from Fig. 9e shows periodic variation of two cycles per day. It is to be noted that the three detector rates (Fig. 9a-c) also show periodic variations of two cycles per day but with a second peak of significantly smaller amplitude. This observation may be understood in terms of the thermal properties of the scintillation detectors and their response to varying atmospheric pressure. A major fraction of the detector rate variation seen in Fig. 9a-c is due to a negative temperature coefficient of the scintillator and the photomultiplier assembly and a smaller fraction is due to the varying absorption of charged particles in the atmosphere. It is interesting to note that the shower trigger rate (Fig. 9d) also shows a periodic variation of two cycles per day but in opposite sense to the pressure change (Fig. 9e).

The pressure wave is produced by a complex interaction of solar heating and the nonlinear response of the upper atmosphere to this forcing. It is well known that the amplitude of the pressure wave depends on the latitude of the site and is larger at lower latitudes. The low latitude location (11.4°N) of Ooty was responsible for the 12 hour periodicity seen in the pressure data (Fig. 9e). The sensitivity of the GRAPES-3 experiment may be gauged from the fact that a small amplitude (~ 1 hPa) pressure wave (~ 0.2 %) significantly modulates the observed rate of showers (~ 1 %). For the sake of clarity the Level-1 shower trigger rate and the pressure data are plotted separately in Fig. 10. A strong anti-correlation between the two parameters is clearly visible. The pressure data shows that the highest values are reached at about 10 h and 22 h local time when the rigger rates reach their minimum values. The coefficient of the anti-correlation is ~ 80 %. This anti-correlation may be explained in terms of a change in the atmospheric absorption of the cosmic ray showers due to this pressure wave. This feature of the GRAPES-3 experiment has turned out to be of critical importance in studying various transient phenomena

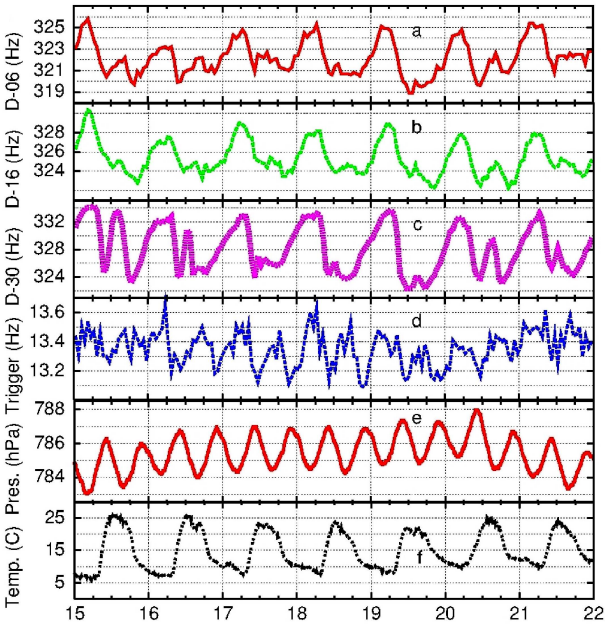

Fig. 9: Observed variation in counting rates for 3 detectors; (a) D-06, (b) D-16 and (c) D-30, recorded using by rate monitoring system and shower trigger (Level-1) rate (d), atmospheric pressure (e), and temperature (f), shown for a period of seven days during 15-22 February 2001

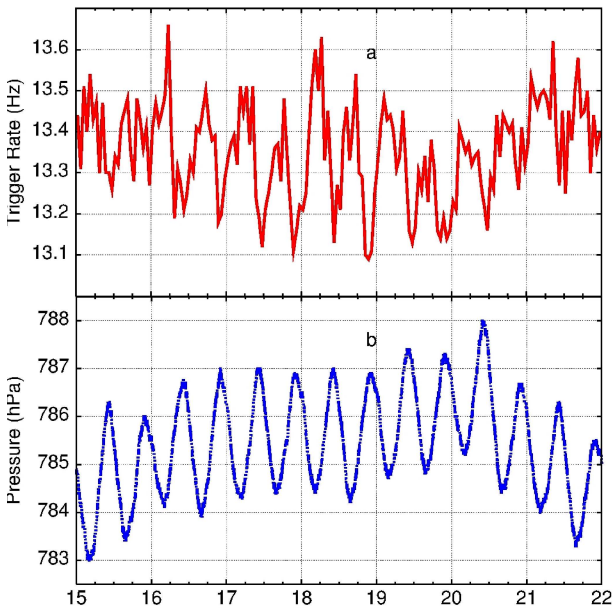

Fig. 10: Pressure observed variation in, (a) shower rate and (b) atmospheric pressure for the seven day period during 15-22 February 2001. 12-hour periodicity seen in pressure and in shower rate data. A high degree of anti-correlation between pressure and showers rate is clearly visible

including those of cosmic, solar or atmospheric origin. The pressure effect is also clearly seen in the muon counting rate [61].

2.6 Muon Detector

As mentioned in §1.5 the muon component has been studied in great detail to obtain unravel the composition of the primary cosmic rays. Proportional counter (PRC) is the basic element of the GRAPES-3 muon detector. The PRC is a 600 cm long, mild-steel, square pipe with a cross-sectional area of 10 cm x 10 cm and a wall thickness of 2.3 mm. A muon detector module with a sensitive area of 35 m^2 consists of a total of 232 proportional counters (PRCs), each with a cross-section of 10 cm x 10 cm, arranged in 4 layers, with alternate layers placed in mutually orthogonal directions. Two successive layers of the PRCs, separated by two 15 cm thick slabs of concrete, permit a 2-dimensional reconstruction of the muon tracks. A separation of 50 cm between the two layers of the PRCs in the same plane, allows the track direction to be measured to an accuracy of 6° in the projected plane. To achieve an energy threshold of 1 GeV for the vertical muons in the EAS, a total thickness ~ 550 g cm^{-2} in the form of concrete blocks is employed as absorber by placing a total of 15 layers of concrete blocks above the Layer-1. This arrangement of the concrete blocks, in the shape of an inverted pyramid provides an energy threshold of sec(θ) GeV, for the muons incident on the detector at a zenith angle of θ. The projection of the concrete shielding on all four sides of the PRCs, as shown in Fig. 11 provides a coverage for the penetrating muons out to 45°. A cross-section of two adjacent muon detector modules is shown schematically in Fig. 11. It needs to be emphasized that the PRCs in the muon detector have to be protected from the high humidity which is typical of the forested area surrounding the GRAPES-3 array. This is necessary to reduce the noise due to potential electrical discharge from the exposed anode wires that are operated at a voltage of 2800 V.

Four modules under common overburden of concrete absorber constitute a supermodule and a cross section of the two modules inside a supermodule is shown in Fig. 11. It is to be noted that the top 7

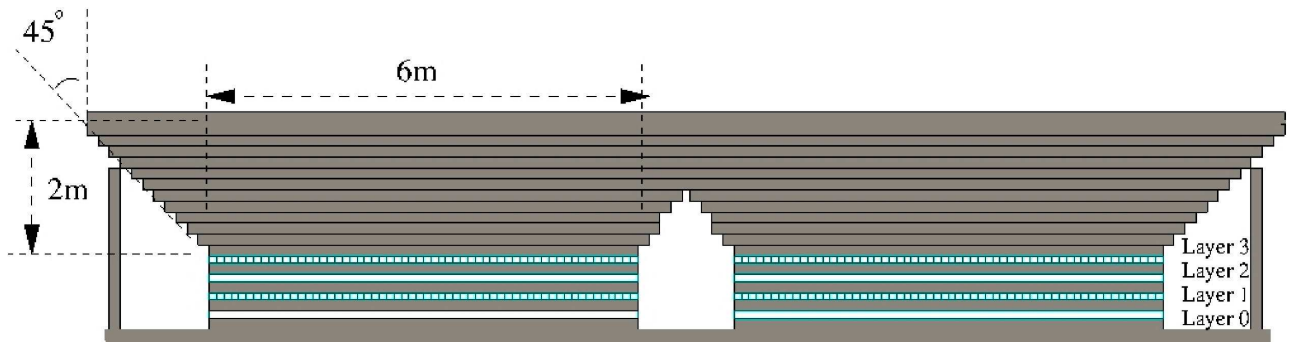

Fig. 11: Schematic view of 2 out of 4 modules in a 4-layer supermodule. A 550 g cm^{-2} thick concrete above Layer-1 ensures threshold, E_μ = sec(θ) GeV for muon arriving with zenith angles θ up to 45°

layers of the concrete blocks are shared as an absorber by all four modules in a super-module. Therefore, the absorber above the 10th layer from the base, is essentially a full-size layer covering all four modules as seen in Fig. 11. Finally, a 30 cm thick and 18 m x 18 m concrete slab was cast as the top layer of the absorber in order to make it weather-proof. Similarly at the bottom, a single 30 cm thick, 16m x 16m concrete block cast on the ground, serves as the floor for the super-module. This was done for uniform distribution of the nearly 1200 tons load of the absorber in a super-module to the soil below. Thus the GRAPES-3 tracking muon detector consisting of sixteen modules of total area 560 m^2, is used for the identification of the multiple muon tracks in an EAS. In the data some of the observed muon tracks could also be due to the accidental coincidences during the latency time of the PRCs and may not have been associated with the detected air shower. To reject such unassociated muons, the arrival time of each muon, called the time offset 'T_0' relative to the EAS trigger is also recorded. The peak in Fig. 13 is due to the muons associated with the EAS, while the tail on both sides of it, is contributed by the accidental coincidence of the unassociated muons. By limiting the value of T_0 between –0.8 to 2.6 μs, the number of the accidental muons was reduced to ≤ 0.2 per EAS.

The PRC wall serves as the cathode and a 100 mm diameter tungsten wire serves as the anode, is mounted at the center of the pipe using hermetic seals. After evacuation, each PRC was filled with P-10 (90 % Ar and 10 % CH_4) gas to a pressure of 24 cm of Hg above local atmospheric pressure and then sealed. The amplitude distribution of the output pulses from each PRC was measured with a multi-channel analyzer. A typical distribution, shown in Fig. 12, displays a prominent peak due to cosmic ray muons corresponding to an energy loss of ~ 20 keV in the 10 cm column of P-10 gas in the PRC. The muon peak is well separated from the other two smaller peaks; the first peak is due to the fluorescent K_α X-ray emission in Fe at 6.4 keV and the second minor peak at 8.6 keV is due to the same effect in the Zn coating on the mild steel pipe, used for its protection from rusting. Any malfunction of the PRC can be easily detected from the change in the shape of this

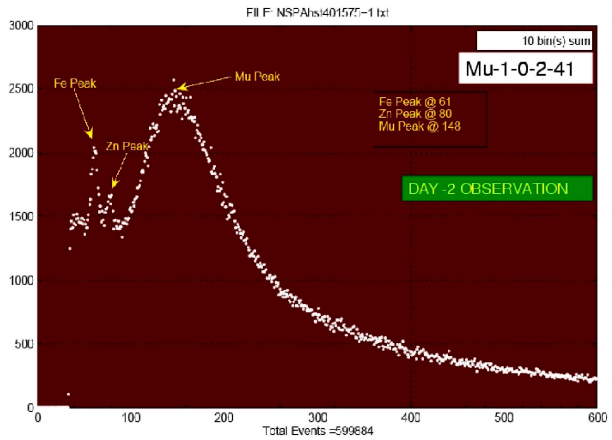

Fig. 12: Pulse-amplitude distribution for a PRC in the muon detector. The first two minor peaks are due to fluorescent K_α X-ray emission in Fe at 6.4 keV (a), and in Zn at 8.6 keV (b). The main peak at ~ 20 keV (c) is due to the passage of cosmic ray muons

distribution and suitable corrective steps can be initiated to restore its performance.

The anode pulse from the PRC was shaped to an exponential form with a decay time of 7 ms and amplified (gain = 83). The amplified pulse was discriminated at a threshold of –100 mV which corresponds to ~ 0.2 of a minimum ionizing particle. The output of the discriminator was a TTL signal. The following information on the discriminator output pulse was recorded; i) the arrival time with a resolution of 167 ns and ii) the width with a resolution of 333 ns. Due to the exponential nature of the amplified pulse, the pulse width is proportional to the logarithm of the PRC pulse amplitude. The number of particles passing through a PRC in a given event are estimated as follows, assuming T_s to be the pulse-width for a minimum ionizing particle, as calculated from the pulse-width monitoring system and τ to be the decay time constant, the number of particles N in an event is given by,

$$N = e^{\left(\frac{Tn-Ts}{\tau}\right)} \qquad (1)$$

where T_n was the pulse width observed for the event. This feature is used to estimate the total number of muons in large multiplicity events.

The maintenance of the stability of gain and detection efficiency of each PRC is an important experimental requirement. In order to monitor the performance of the muon detector, the pulse-width of all 3712 PRCs is continuously measured with a Pulse Width Analyzer system. It is to be noted that as a result of the exponential shaping of the PRC pulse and subsequent measurement of its width, the number of 'equivalent' minimum ionizing particles entering a PRC are effectively digitized to a precision of ~ 5 % for 1 to 5 particles and ~ 10 % for more than 5 particles. The shape of the pulse-width distribution is utilized to detect noisy and/or leaky PRCs. The 6.4 keV fluorescent K_α X-ray emission peak in Fe is used for calibration and monitoring of the gain of the PRCs. In addition, the counting rates of any 3-layer and all 4-layer coincidences between Layer-OR signals are also monitored continuously to provide information on the health of the muon detector.

Since the shower muons are also aligned along the direction of the EAS, a further removal of the accidental muons was achieved by reconstructing the direction of the muon tracks in two mutually orthogonal vertical projection planes (X-Z and Y-Z, where Z is the vertical direction), by employing the tracking capability of the muon detector. The procedure used is as follows, first the projection angles of the air shower are calculated for these two orthogonal planes. Next, in each projection, the reconstructed muon track is required to lie within 10^0 of the EAS direction for it to be considered a shower muon. The number of the shower muons are independently determined for each projection plane and the larger of the two is treated as the true number of the shower muons in a given module. The total number of detected muons is obtained by summing the number of muons in all sixteen modules. Therefore, the twin criteria of restricting the time offset and the direction allows a relatively clean identification of the shower muons to be made. The estimate of the number of muons through the reconstruction of individual tracks is fairly reliable for a relatively small number of tracks in a given module. However, as the number of muon tracks in a module increases, these tracks start to overlap and their number gets underestimated. This saturation effect in a 35 m^2 module was investigated through the Monte Carlo simulations and the results obtained are displayed in Fig. 14.

For example, on an average 10 incident muon tracks actually get reconstructed as only 8 tracks. Since there are sixteen modules this effect becomes significant for muon multiplicities of = 150. However, this saturation effect is automatically accounted for, since the shower simulation code used here also includes the true reconstruction capability of the muon detector. In the analysis of the real data, the showers with cores landing between 60 and 80 m from the center of the muon detector were selected as is shown in Fig. 3. This was done not to mitigate the above mentioned saturation effect, but to minimize the probability of the incidence of the penetrating hadrons in the muon detector.

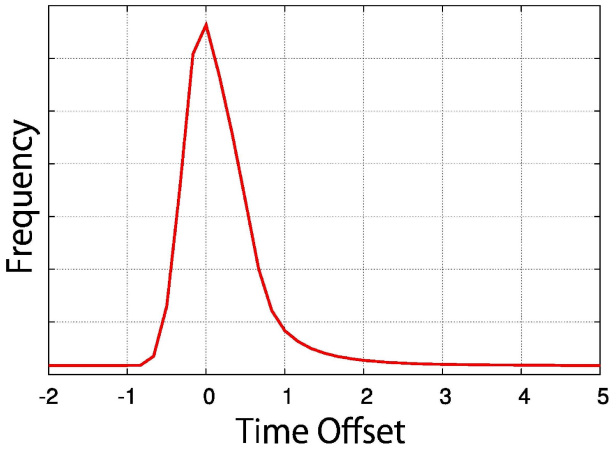

Fig. 13: Distribution of the muon time offset T_0 in ms

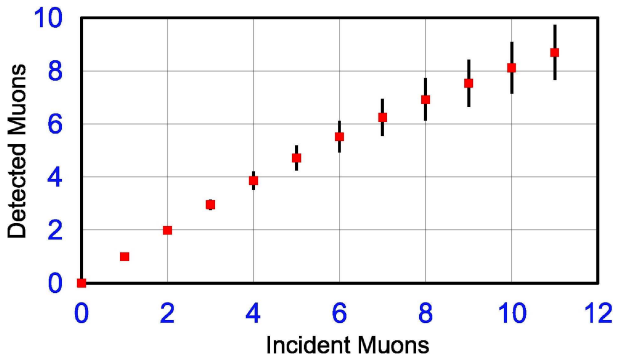

Fig. 14: Mean number of reconstructed muon tracks as a function of number of incident muons estimated from simulations

The GRAPES-3 trigger was optimized for the selection of low energy EAS, by requiring a 3-fold coincidence between the detectors on the adjacent lines, formed by the inner 127 detectors located inside the dashed hexagon shown in Fig. 3. In addition, a minimum of ≥ 10 detectors were required to be triggered, each with a signal equivalent to ≥ 30 % of a minimum ionizing particle. The arrival time and the charge in the PMT pulse were recorded for all detectors, for the subsequent determination of the arrival direction (θ, ϕ) and the shower size (N_e) [60]. The Monte Carlo simulations of the EAS initiated by the primary cosmic rays, using the CORSIKA code, for the five nuclei, namely, H, He, N, Al and Fe had shown that a triggering efficiency of ~ 90 % is obtained at a primary energy of 50 TeV for the H, which increases with the atomic mass, eventually reaching a value of 100 TeV for the Fe primaries [60].

For every EAS trigger, the following information was recorded for each PRC in the muon detector; (i) the arrival time of the digital pulse, formed by an amplifier-discriminator module, with a time resolution of 167 ns, and (ii) the pulse width with a time resolution of 333 ns. Due to the exponential nature of the amplified pulse, the pulse width is proportional to the logarithm of the pulse amplitude. The arrival time of the pulse was used for the rejection of the PRCs that may have fired accidentally during its latency time as explained earlier. In Fig. 15 the observed muon tracks in one out of sixteen modules are shown. Two distinct tracks are clearly visible in each of the two orthogonal projections. In most cases the individual muon tracks are readily identified, except when the track multiplicity becomes very high. The lateral density distribution of the detected charged particles in a typical shower is shown in Fig. 16. As expected, a large number of particles are detected near the core

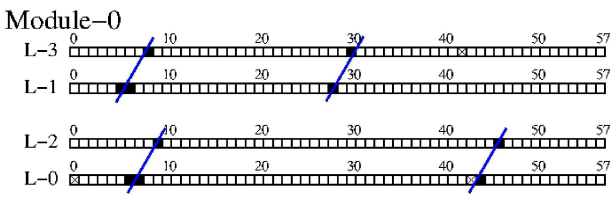

Fig. 15: Muon tracks in a 35 m^2 module

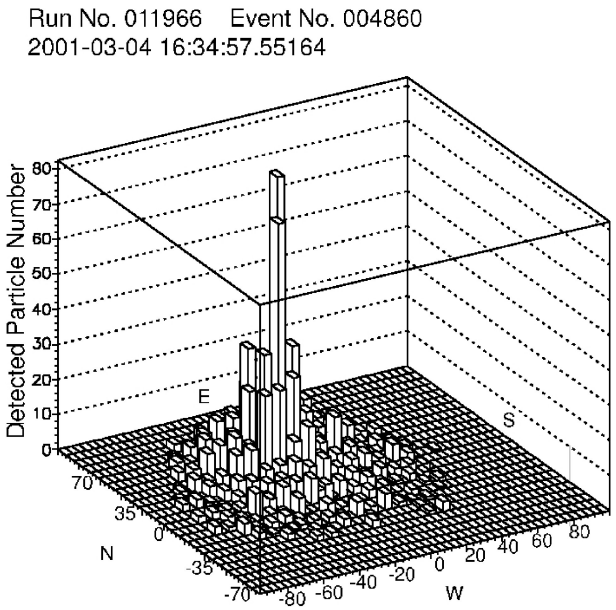

Fig. 16: Number of detected particles observed in an EAS. Height of each tower proportional to particle density in corresponding detector

of the EAS, and their density falling off rapidly away from the core of the EAS.

3. Cosmic Ray Composition

Some of our earlier results [10] based on the Monte Carlo simulations had indicated that the shape of the muon multiplicity distribution (MMD) measured with a large area muon detector was a sensitive probe of the relative mix of different nuclei in the primary cosmic ray flux [89]. Following this indication, we have attempted to extract the energy spectrum of the protons and other nuclei through a comparison of the observed MMDs with the expectations from the Monte Carlo simulations, for different models of hadronic particle interactions as discussed in the subsequent sections. Some of the key shower parameters at the atmospheric depth of the experiment, namely, the lateral distribution is used to fit the shower core and size. The errors in the core location and shower size have been studied as a function of the shower size. The dependence of the differential shower size spectra at different zenith angles etc., has also been studied. Using these distributions the vertical flux is derived for further analysis.

A total of 6 x 10^8 showers collected over a total live time of 4.7 x 10^7 s (545 d), spread over the 3-year period, 2000-2002, were analyzed for determining various shower parameters, namely, the arrival direction, defined by the zenith (θ) and the azimuthal (Φ) angles, the shower size (N_e), the core position (x_c, y_c) and the shower age (s). These shower parameters are described, subsequently, in greater detail. For each shower, the zenith angle θ and the azimuthal angle are determined by using the timing information from the Time to Digital Converter (TDC) from each detector. The angular resolution of the shower array was estimated by using three different methods, namely, the even-odd, the left-right as well as from the observations of the shadow of the Moon on the isotropic flux of the cosmic rays. The angular resolution was estimated to be 0.7° for the showers of size $N_e \geq 10^4$ particles [76]. In the present work, only the showers with the zenith angle $\theta < 45^0$ and with cores landing within 30 m from the center of the array, as shown in Fig. 3, were selected for further analysis as described below in detail.

As a first step, the approximate position of the shower core is estimated from the weighted mean of the location of the detectors with the 7 highest detected particle densities, where the weights are the measured particle densities in those 7 detectors. Next, the shower direction, namely, the zenith angle θ and the azimuthal angle Φ are calculated by a χ^2 minimization of the relative arrival times of the detected particles. The shower size is a critical parameter for the present work and it was carefully estimated from the lateral distribution of the charged particles by fitting them to the Nishimura-Kamata-Greisen (NKG) lateral distribution function. The age (s) of the shower represents the steepness of the lateral distribution function [77], and it was calculated by using the maximum likelihood algorithm MINUIT. The details of the analysis procedure are described below.

If n_i particles pass through the detector labeled i, located at (x_i, y_i), which has detected S_i particles, then the expected particle density ρ_i is calculated as follows :

$$r_i = \sqrt{(x_i - X)^2 + (y_i - Y)^2 - D^2} \tag{2}$$

$$D = (x_i - X)\sin\theta Cos\phi + (y_i - Y)\sin\theta\sin\phi \tag{3}$$

$$\rho_i = C\left(\frac{r_i}{r_m}\right)^{s-2.0}\left(1+\frac{r_i}{r_m}\right)^{s-4.5} \tag{4}$$

$$C = \frac{N}{2\pi r_m^2}\frac{\Gamma(4.5-s)}{\Gamma(s)\Gamma(4.5-2s)} \tag{5}$$

where, r_m is the Moliere unit and r_m = 103 m, for the atmospheric depth at Ooty. For an incident particle density ρ, the probability of detecting n_i particles is ρ_i, then the probability of such a detection is L which may be derived from the following equations,

$$p_i = \frac{(\rho_i S_i \cos\theta)^{n_i}}{n_i!} e^{-\rho_i S_i \cos\theta} \tag{6}$$

$$L = \Gamma_i \, p_i \tag{7}$$

The increase in the path length for the zenith angle θ is considered in the above calculation when estimating n_i. The unknown parameters are determined by maximizing L. The initial values for these parameters are set by using the following relations,

$$R_{core} = \frac{\sum High\ 7 n_i r_i}{\sum High\ 7 n_i} \tag{8}$$

$$N_e = 102[n_i]^{0.97} \tag{9}$$

$$s = 1.0 \tag{10}$$

In the equation 8 the core location is obtained by calculating the mean location, weighted by the detected particle density of the 7 detectors with the highest density. The approximation described in equation 9 was originally obtained through the Monte Carlo simulations. Since the detector response becomes non-linear when the detected particle density $\rho_i S_i sec(\theta)$ exceeds 200, such detectors are not included in the NKG fit. If the probability ρ_i for a

particular detector *i* is less than 10^{-4} of the expected value, then also that detector is rejected from further calculations.

The accuracy of the core location is estimated by using the Monte Carlo simulations. The protons are injected as the primary cosmic ray particles and the error in the location of the shower core is calculated by using the CORSIKA code and the same reconstruction procedure as was used for the real data. Next, the distance Dr between the original and the reconstructed shower core locations is calculated. The estimated mean error Δr_m in the shower core location varies from ~ 1.6 m at a shower size of $10^{4.3}$ to about ~ 0.6 m at a shower size of $10^{5.2}$. The accuracy of the shower size determination has also been estimated through the Monte Carlo simulations using the CORSIKA code. In these simulations the protons are injected as the primary cosmic rays and the shower size N_{fit} is estimated by fitting the NKG function to the lateral density distribution of the particles in the simulated EAS. For the shower size range $10^{4.4} \leq N < 10^{5.2}$, the rms errors are found to be smaller than 10 % for the simulated showers.

The observed differential shower size (N_e) spectra for different values of the zenith angle θ, grouped in bins of sec(θ) of width 0.05, are shown in Fig. 17. It is to be noted that the flux values shown on the Y-axis have been multiplied by a factor of $N_e^{2.5}$, to achieve better clarity in the presentation. It also needs to be emphasized that the statistical errors on the data points shown in Fig. 17 are very small. This is due to the fact that there are more than 10^5 showers in each N^e, sec(θ) bin. A comparison of the shapes of these nine spectra for the sec(θ) varying from 1.025 (middle value for the first bin, θ ~ 13°) to 1.425 (for the ninth bin, θ ~ 45°), clearly demonstrates the close similarity among them, apart from the differences in the magnitude of the flux values. Since the spectral slope is independent of the zenith angle θ, it was decided to combine the data of all showers with sec(θ) < 25^0, after suitable normalization for further analysis of the muon content of the EAS. The vertical flux shown in Fig. 17 is derived from the showers with zenith angles θ < 25° and converted into equivalent vertical size by using the following relation,

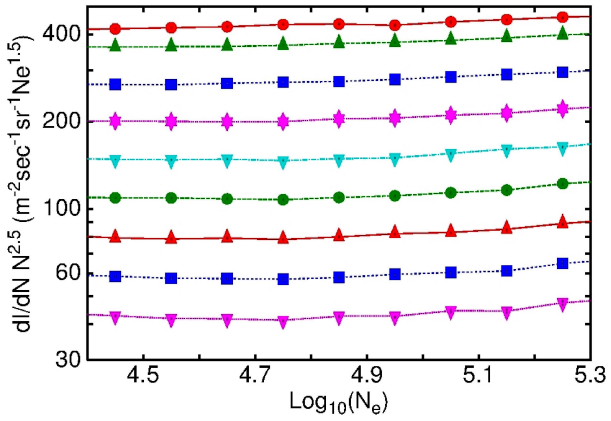

Fig. 17: Observed differential size (N_e) spectra for sec(θ) intervals of 0.05. Top plot (red ●) vertical direction, second plot (green ▲) 1.00 < sec(θ) < 1.05, …, last plot (magenta ▼) 1.35 < sec(θ) < 1.40

$$N(0) = N(\theta) e^{\frac{Xv}{\lambda}(\sec\theta - 1)} \qquad (11)$$

where vertical depth X_n and the attenuation length λ are 800 g cm^{-2} and 200 g cm^{-2} respectively.

The number of muons observed in the sixteen modules of the muon detector are counted after reconstructing the tracks in both of the orthogonal projections, based on the hit pattern observed in the four layers of the PRCs. A muon which is outside the time window from –0.8 to 2.6 ms, relative to the accompanying shower or whose projected direction is more than 10° away from the shower direction in any one of the planes is rejected as due to the background flux of the atmospheric muons. In addition, only the showers whose cores lie between 60 and 80 m from the center of the muon detector and are also within the 30 m radius circle around the center of the GRAPES-3 array are analyzed. This kidney shaped area for the selection of the showers, is shown as shaded in Fig. 3.

The distribution of the number of detected muons is referred to as the observed muon multiplicity distribution, hereafter referred as the MMD. The MMDs shown in Fig. 21 are for two different size groups, namely, $10^{4.4} \leq N_e \leq 10^{4.6}$ and $10^{5.0} \leq N_e \leq 10^{5.2}$, respectively for hadron interaction generator QGSJet. Similar MMDs were also obtained for the remaining seven shower size groups, whose size spectra were shown in Fig. 17. These MMDs were used for

determining the energy spectra and the relative proportion of various nuclear groups in the primary cosmic ray flux. This was accomplished by a comparison of the observed MMDs with the expectation from detailed Monte Carlo simulations using the CORSIKA code [79] and the detector response using GEANT4 [60], following the selection of a suitable generator for the hadronic interactions as discussed below.

3.1 Monte Carlo Simulations

Most of the ground based observations of the extensive air showers record the presence of the hadrons, the electrons, the muons and other components deep down in the atmosphere, after nearly 8-10 mean free paths for the interaction of high energy particles [91]. Therefore, the detected flux of particles at the observational level is the end product of hundreds of interactions at different depths in the atmosphere. Thus, the extraction of the information on the primary cosmic rays and the characteristics of the first few ultra-high energy interactions necessarily requires a comparison of the observations with the expectations from the Monte Carlo simulations, using the models of particle interactions for an assumed primary cosmic ray flux, energy spectrum and composition. Since the extreme forward region of the particle interactions in the laboratory frame can not be studied, in the high energy collider experiments, the models of the high energy interactions need to be necessarily extrapolated from the energies of a TeV to as high as a 1000 TeV and beyond.

Since some of the parameters used to describe the hadronic interactions in the CORSIKA Monte Carlo simulations are extrapolated from the lower energy measurements, a significant model dependent uncertainty in the results of these simulations is naturally to be expected. The CORSIKA code version 6.020 (2003-March-24) has several built-in hadronic interaction generators [80, 81] and the ones considered here include the quark-gluon string based QGSJet [82], the dual parton with mini-jet based SIBYLL [83, 84], the NeXus [85] generators. The interactions of the low energy hadrons (< 80 GeV) were treated using the GHEISHA generator [86].

In the CORSIKA code, the electromagnetic cascade can be treated by two different methods, namely, the EGS4 code [87] or the NKG function [77, 78]. The EGS4 code individually tracks each electromagnetic particle in a given cascade. However, the NKG function only calculates the density distribution at the observational level and therefore, proceeds much faster than the EGS4 code. To save the computation time, we had decided to use the NKG function. However, we had also performed simulations using the EGS4 code for a limited number of events, in order to investigate the differences between the results obtained from these two methods, after folding the detector response using the GEANT4 code [60, 88]. In particular, the saturation effects on the number of observed muons at high multiplicities were properly accounted for. This comparison showed that the results were relatively insensitive to the specific method used.

For the sake of simplicity, the primary flux was assumed to be composed of only five species, namely, the protons (H, A=1), the helium (He, A=4), the nitrogen (N, A=14), the aluminum (Al, A=27) and the iron (Fe, A=56). In the simulations of the EAS, the primary cosmic ray energies were randomly selected from a power-law energy spectrum of slope –2.7 for the five nuclei, namely, H, He, N, Al, and Fe with threshold energies that are summarized in Table 4. These thresholds were selected to be sufficiently small such that the efficiencies are < 10 % for the generation of the GRAPES-3 trigger [60]. The core of the simulated showers were thrown randomly over an area of radius 100 m around the centre of the array. The simulated showers were subjected to an analysis procedure identical to the one used for the observed showers. First, it was checked if the criterion for the

Table 4: CORSIKA simulation parameters

Nucleus	Mass (A)	Charge (Z)	Energy (TeV)
H	1	1	5
He	4	2	8
N	14	7	16
Al	27	13	16
Fe	56	26	20

GRAPES-3 trigger is met and only then the EAS parameters, such as the shower size and the muon multiplicity of the simulated shower were calculated for obtaining the simulated MMD. Since there is significant overlap between the MMDs for the Al and the Fe groups, thus these two species have been combined by assuming an abundance ratio (Al/Fe) of 0.8 based on one of the direct measurements [99]. Since the abundance ratio Al/Fe was fixed, therefore, effectively the number of independent mass species were reduced to four resulting in a relatively rapid convergence during the minimization procedure. Only the showers arriving at a zenith angle of $\leq 30^{o}$ were simulated. All hadrons and muons in the shower were tracked until their energy dropped to 1 GeV.

The simulated MMDs for each of the five nuclei were normalized per shower and the contribution a_i of each nuclei is extracted from the minimization of the χ^2 using MINUIT minimization program to reproduce the observed MMD for each shower size N_e bin.

$$\chi^2 = \sum_k \frac{\left(n_{0k} - \sum_i a_i n_{ik}\right)^2}{\varepsilon_{0k}^2 + \sum_i (a_i \varepsilon_{ik})^2} \qquad (12)$$

where, k is the bin number of the multiplicity, i represents different mass groups in used the simulations, for example, $i = 1 \sim 5$ refers to proton, helium, nitrogen, aluminum and iron respectively, and $i = 0$ refers to the observational data. n_{ik} and ε_{ik} are the mean frequency and the corresponding statistical error in the k-th bin. Initially the magnitude of the free parameters a_i were set to 0.2 and the effect of the initial values on the final result was found to be negligible.

It has been pointed out by the CORSIKA development team [79] that different models of fragmentation of the incident nucleus, from a full fragmentation in the first interaction (superposition model), to a partial fragmentation into other nuclei and their subsequent interactions, lead to essentially the same results for most of the observables deep down in the atmosphere, where the observations are made. Various distinctive features of the fragmentation are smeared out by the occurrence of large fluctuations in the huge number of individual interactions, during the development and propagation of the shower in the atmosphere. Therefore, we decided to use the simpler superposition model and treat the interactions of an incident nucleus of atomic mass 'A' as the superposition of the interactions of A incident nucleons, from the first interaction.

Before going into a detailed comparison of the observed MMDs for the various shower size groups, with the results from the Monte Carlo simulations, it is useful to familiarize with some of the broad features of the predictions from different models. For example, on an average, the QGSJet generator predicts a smaller shower size at the observational level as compared to the other two generators, namely, the SIBYLL and the NeXus. Thus the QGSJet requires a relatively higher primary energy to generate the same observed shower size. This is clearly visible from the distributions of the simulated shower size for the H and the Fe nuclei, for the primary energies of 100 TeV, as seen from Fig. 18a-b. The ratio of the shower sizes for H and Fe at 100 TeV is ~ 3. A very similar result is obtained at 1000 TeV as seen from Fig. 18c-d. As compared to the QGSJet results, the shower size is about 10 % larger for the SIBYLL generator and is the largest for the NeXus generator.

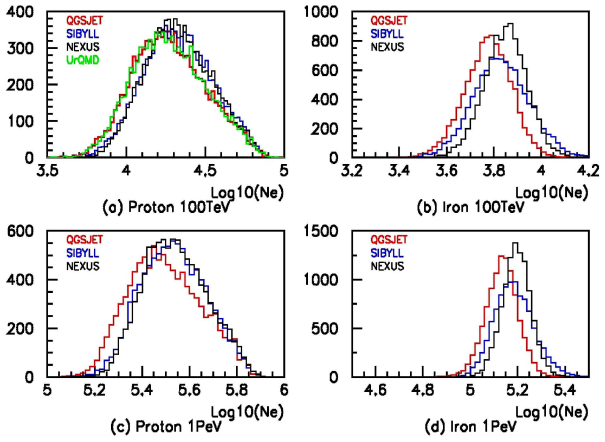

Fig. 18: Distributions of shower size for various interaction generators; (a) 100 TeV H, (b) 100 TeV Fe, (c) 1000 TeV H, (d) 1000 TeV Fe

A similar comparison of the distributions of the number of muons of energy > 1 GeV, the so called 'muon size' N_μ, in the showers initiated by H and Fe nuclei for three different hadronic interaction generators, namely, the QGSJet, the SIBYLL, and the NeXus is shown in Fig. 19a-d. It is interesting to note that the trend is reversed for the muon size N_μ, as compared to the electron size N_e, for these three hadronic interaction generators. The muon size, on an average, is significantly larger for the QGSJet generator as compared to the SIBYLL or the NeXus generators. This reversal further enhances the differences in the MMDs when the showers of the same electron size N_e are compared.

Since the muon multiplicity in the 560 m^2 area muon detector at a well-defined distance from the shower core is a key observable in the GRAPES-3 experiment, it is relevant to compare the expected muon lateral distributions for different interaction models. This comparison is displayed in Fig. 20a for the showers that were initiated by 100 TeV protons. The variation in the ratio of the expected muon densities for different generators, namely, the SIBYLL and the NeXus with the radial distance, relative to the QGSJet generator is shown in Fig. 20b. It is seen that the expected density for the SIBYLL and the NeXus generators is ~ 10 % smaller as compared to the QGSJet generator. However, the NeXus generates a broader muon lateral distribution as compared to the other two generators. Here, we had used the GHEISHA 6.00 hadronic interaction generator [86] at energies ≤ 80 GeV.

3.2 Composition Results

Since one of the main objectives of the GRAPES-3 experiment is to compare the absolute flux and the energy spectra extracted from the MMDs with the results from the direct measurements, the number of simulated showers were normalized to the number expected during the actual observation time of 4.71 x 10^7s used in the present analysis. The number of detected showers in a size group on the average, are heavily weighted in favor of protons and other lighter nuclei, due to a relatively larger shower size, as compared to the heavier nuclei of the same primary energy as discussed earlier. This is shown clearly for H and Fe at 100 TeV in Fig. 18a-b and at 1000 TeV in Fig. 18c-d. The ratio of the sizes is ~ 3 for H and Fe at these energies.

The observed MMD for the showers in the size range $10^{4.4}$-$10^{4.6}$ is shown in Fig. 21a. Also shown in the same figure are the results of the simulated EAS initiated by H, He, N, Al and Fe nuclei, using the QGSJet generator. It is to be noted that the relative

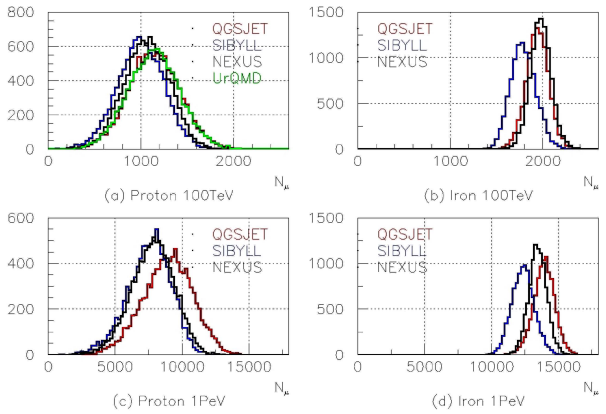

Fig. 19: Distributions of N_μ i.e. number of ≥ 1 GeV muons, for QGSJet, SIBYLL, NeXus generators; (a) H at 100 TeV, (b) Fe, at 100 TeV (c) H at 1000 TeV, (d) Fe at 1000 TeV

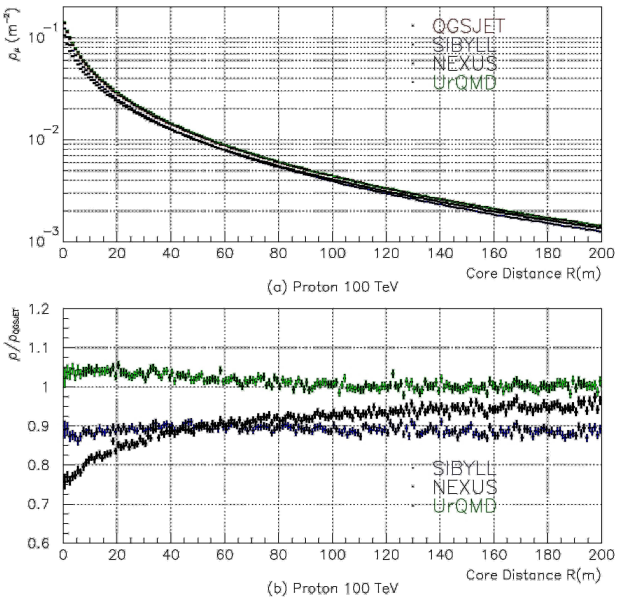

Fig. 20: A comparison of lateral distributions for ≥ 1 GeV muons for different interaction generators for 100 TeV proton showers, (a) QGSJet, SIBYLL, NeXus. Ratio of muon density, (b) SIBYLL, NeXus relative to QGSJet

abundances of the 4 primary groups (Al/Fe ratio being fixed at 0.8) have been obtained from a χ^2 minimization for the fit between the observed distribution and the sum of the 4+1 distributions is displayed in Fig. 21a. It is interesting to note that the summed distribution, also shown in Fig. 21a gives a good fit to the observed distribution for the full range of muon multiplicity, from 1 to 30 muons. A similar comparison of the same observed muon distribution with the summed distribution expected for the SIBYLL generator is also shown in Fig. 22a. The summed muon distribution shown in Fig. 22a, also yields an equally good fit to the observed muon distribution, although with different relative abundances of various nuclear groups.

However, from a comparison of the data displayed in Fig. 21a and Fig. 22a, it is clearly seen that relatively fewer heavier nuclei are required to fit the large ($n_\mu > 20$) multiplicity region for the QGSJet as compared to the SIBYLL generator. It is also of interest to note that the small ($n_\mu > 10$) multiplicity region is entirely accounted for, by the showers due to the lighter nuclei. Dominance of different mass groups at different muon multiplicities clearly indicates the sensitivity of this technique to the nuclear composition of the primary cosmic rays. These two sets of plots in Figs. 21a, and 22a also show a clear evidence of the presence of the heavier nuclei in the primary flux at energies responsible for the generation of the showers in the size range, $10^{4.4}$-$10^{4.6}$. This comparison also shows that the interpretation of the same data requires significantly different composition for the QGSJet and the SIBYLL generators.

In Figs. 21b 22b the observed MMDs for the showers in the size range $10^{5.0}$-$10^{5.2}$ are shown for the QGSJet and the SIBYLL generators, respectively. The muon multiplicities are significantly larger for this shower size range and extend from 1 to 60. A similar analysis using the simulations with the same five components, shows that for this shower size range also, the QGSJet generator requires a relatively small contribution of the heavier nuclei for the interpretation of the data as shown clearly in Fig. 21b. On the other hand the same analysis requires the presence of a substantial contribution of the heavier nuclei for the reproduction of the observed MMD using the SIBYLL generator as seen from Fig. 22b.

The discussion above, using the MMDs for two different shower size ranges clearly demonstrates that the derived composition of the primary cosmic rays is intricately linked to the selection of the hadronic interaction generator. Since it is not possible to unambiguously identify a unique hadronic interaction generator from the present analysis of the GRAPES-3 MMD data, we had to resort to other constraints to select an appropriate generator.

Following the procedure outlined above, the relative abundances of the four primary groups, were determined from the simulations using the QGSJet generator. This was done for each of the five shower size groups, namely, $10^{4.2}$-$10^{4.4}$, $10^{4.4}$-$10^{4.6}$, $10^{4.6}$-$10^{4.8}$, $10^{4.8}$-$10^{5.0}$ and $10^{5.0}$-$10^{5.2}$. The variation in the relative abundance for the four primary groups with shower size, over the size range, $10^{4.2}$-$10^{5.2}$, is shown in Fig. 23 labeled 'Q'. The results obtained from a similar analysis using the SIBYLL generator are shown labeled 'S' in Fig. 23. As mentioned earlier, different shapes of the MMDs as seen in Fig. 21, 22 yield significantly different abundances for the QGSJet and the SIBYLL generators, respectively.

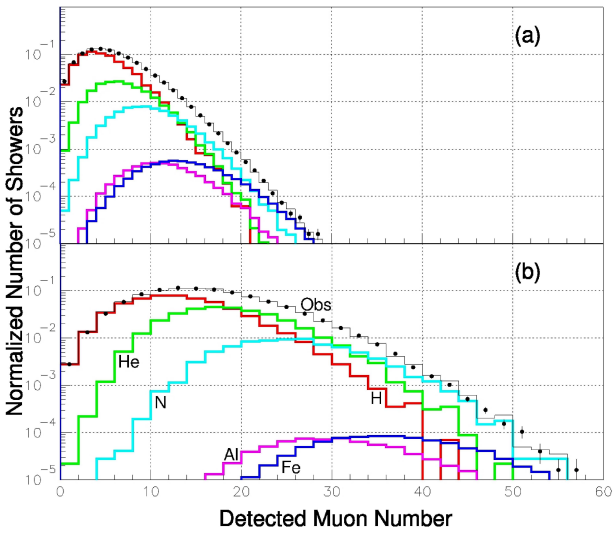

Fig. 21: Comparison of observed MMDs for EAS in shower size ranges, (a) $10^{4.4}$-$10^{4.6}$ (b) $10^{5.0}$-$10^{5.2}$ with simulations of EAS by H, He, N, Al and Fe nuclei using QGSJet. Summed histogram obtained after χ^2 minimization

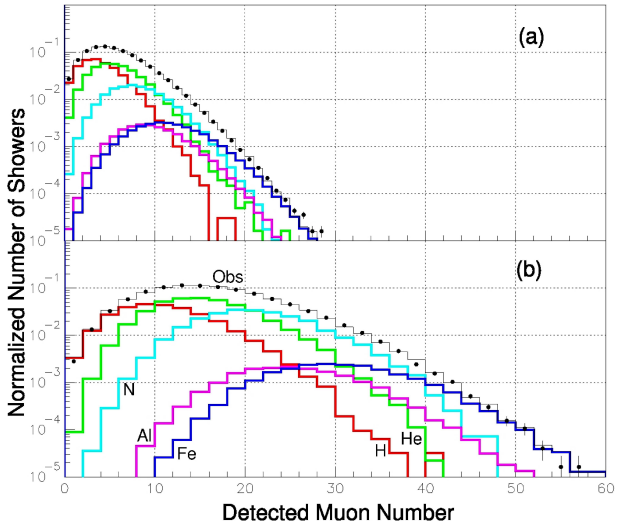

Fig. 22: Comparison of observed MMDs for EAS in shower size ranges, (a) $10^{4.4}$-$10^{4.6}$ (b) $10^{5.0}$-$10^{5.2}$ with simulations of EAS by H, He, N, Al and Fe nuclei using SIBYLL. Summed histogram obtained after χ^2 minimization

It is rather interesting to compare these results on the relative abundances for these two interaction generators, since they also yield substantially different trends for the size dependence of the composition of the primary cosmic rays. On the one hand, the H are much more abundant while using the QGSJet, as compared to the SIBYLL generator. These Monte Carlo simulations show that the H showers generated using the QGSJet have ~ 15 % more muons as compared to those generated using the SIBYLL, for the same primary cosmic ray energy. This is also reflected in the results shown in Fig. 23 where the H fraction for the QGSJet is > 70 % at $N_e = 10^{4.3}$. However, thereafter the H fraction decreases with increasing shower size N_e, for both the generators, thereby suggesting a steeper energy spectra for the H, as compared to the other nuclei. It is specially significant that the abundance of the H sharply decreases by ~ 30 % from $N_e = 10^{4.3}$ to $N_e = 10^{5.1}$ for both the QGSJet and the SIBYLL generators.

On the other hand, the fraction of He increases with increasing size for the QGSJet, while it stays almost constant for the SIBYLL generator. Interestingly, exactly reverse size dependence is observed for the fraction of N, wherein this fraction increases with the increasing size for the SIBYLL, while it is almost size-independent for the QGSJet generator. More significantly, the heavy nuclei (Al+Fe) fraction is relatively large for the SIBYLL as compared to the heavy fraction for the QGSJet generator. It is to be noted that even a small fraction of ~ 5 % for the (Al+Fe) component for a given size group corresponds to a much larger ($\geq$ 15 %) fraction in the corresponding primary energy range. This is due to the well-known fact that the EAS initiated by the heavy nuclei develop much faster in the atmosphere, reaching their maximum size higher up in the atmosphere and then attenuating faster in the lower atmosphere prior to their detection. This leads to a size at the observational level which is almost one-third of the size for a H-initiated shower of the same primary energy. Of course, as mentioned earlier the heavy nuclei component is much smaller for the larger size groups for the QGSJet generator. These results have significant implications for the nature of the sources of the primary cosmic rays and the acceleration processes that are dominant over the energy region 100-1000 TeV [92, 93].

For a direct comparison, the observed N_e spectra have to be converted into energy spectra for the five nuclear groups. Taking into account the exposure factor of the data used for the MMDs, for example, those shown in Fig. 21 and Fig. 22 for a given size group and for the two interaction generators, it is relatively straightforward to convert the relative abundances that were shown in Fig. 23 to the flux values for various nuclear groups at a median primary energy relevant for that particular size group. The mean energy for each logarithmic N_e bin is computed from the primary energy of the showers included in that bin, after imposing the selection cuts discussed above.

Thus a median primary energy is assigned to the each shower size group, using the size-to-energy relations derived from the Monte Carlo simulations for the five primary nuclear groups and for the two interaction generators. The relation between the median primary cosmic ray energy $\langle E_0 \rangle$ and the median shower size $\langle N_e \rangle$ for the five nuclear groups for the QGSJet generator is shown in Fig. 24. To obtain this relationship we have used the Monte Carlo

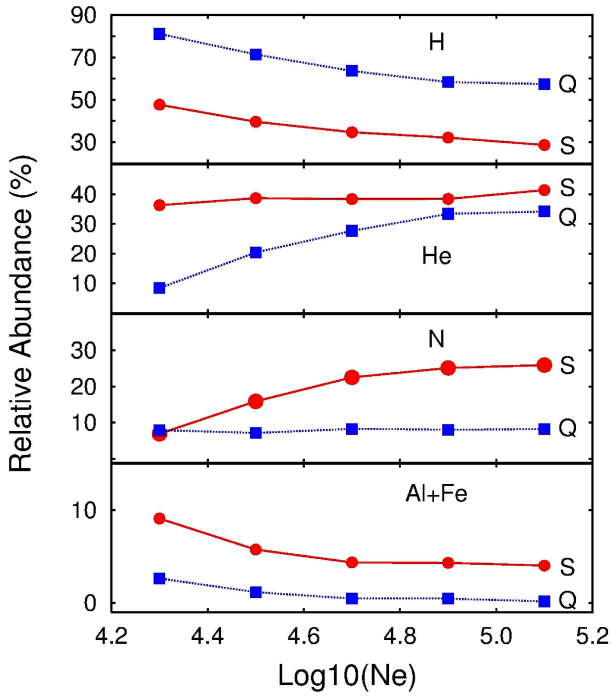

Fig. 23: Relative abundances of 4 primary nuclear groups with shower size for QGSJet (Q) and SIBYLL (S) interaction generators

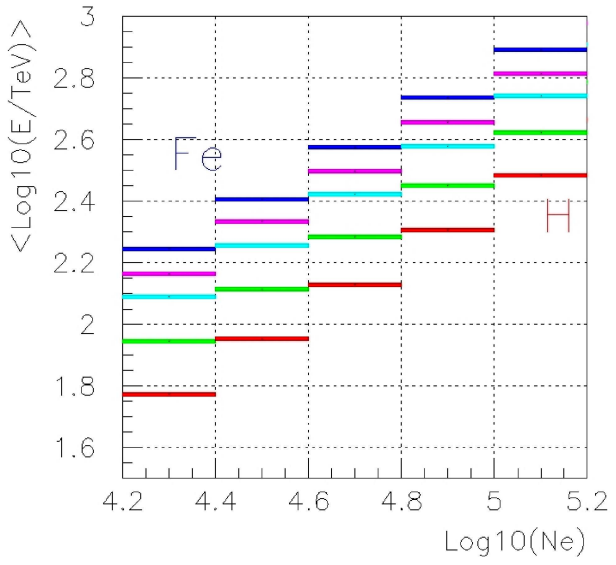

Fig. 24: Relation between mean primary cosmic ray energy and shower size for H and Fe primaries from simulations using SIBYLL

simulated MMDs with the same slope of energy spectra and applied the same cuts as in the experimental data, including the trigger, the core location etc. The shower size is converted into energy through this relationship. Similar relationship for the SIBYLL generator, between the shower size and the median energies was also obtained. The energy spectra so derived are compared with the results obtained by other groups as shown in Fig. 25. The H and He data are taken from [94, 95, 98-100] and the N, Al and Fe data from [5, 95, 99, 100].

The energy spectra for the H and the He nuclei, are shown in the top and second panel of Fig. 25, for the two interaction generators, namely, QGSJet (blue ■) and SIBYLL (red •). The spectra obtained for the other three nuclear groups namely, N, Al and Fe are shown in Fig. 25 in the third, fourth and fifth panels, respectively. Here, it may be reiterated that the spectra for the Al and Fe groups have an identical shape since the relative abundance was assumed to be 0.8 for these two groups. They have been plotted separately here to facilitate a comparison with the results from the direct measurements, which are also displayed in Fig. 25.

A good agreement on the nuclear composition and the energy spectra of the primary cosmic rays between the GRAPES-3 results and the direct measurements is clearly seen when the SIBYLL generator is invoked, particularly with the JACEE and the SOKOL results [95, 98]. The comparison with the direct measurements show that the SIBYLL generator seems to provide a significantly better description of the hadronic interactions in the overlap energy region from 100 to 300 TeV. These are absolute fluxes as they were derived from the shower size N_e and the MMD directly, without recourse to any other flux normalization. The extension of the energy spectra by a factor of ~ 3, for the five nuclear groups provided by the GRAPES-3 experiment is consistent with an extrapolation of the spectra measured by the direct methods. Although, the shower size N_e spectra shown in Fig. 17 can be fitted to a single power law, however, when it is combined with the MMDs, different spectral slopes emerge for the five nuclei as shown in Fig. 25.

The consistent results obtained using the SIBYLL generator with the direct measurements, underscores the utility of the energy overlap in the

selection of the appropriate generator. A comparison of the GRAPES-3 all-particle energy spectrum with the direct observations [94-96, 98-100] as seen in Fig. 26 also display good agreement, except for the RUNJOB results [99]. However, this comparison of the all-particle spectra does not allow any distinction to be made between the QGSJet and the SIBYLL generators.

An analysis of 6 x 10^8 extensive air showers and associated muon content as measured in the GRAPES-3 experiment, has been used to obtain the muon multiplicity distribution as a function of the shower size N_e in the range $10^{4.2}$-$10^{5.2}$, which corresponds to the energy range 100-1000 TeV. A comparison of the energy spectra for the H and the other four nuclear groups obtained using the MMDs, with the direct measurements as shown in Fig. 25, demonstrates the inadequacy of the QGSJet generator to provide a good agreement. On the other hand, the SIBYLL generator leads to a significantly better agreement between the results from the GRAPES-3 and the direct experiments. This observation is specially relevant for the comparison of the H spectra for the following two important reasons, (i) the flux values from the direct measurements are intrinsically more reliable, especially at the lower end of the overlap energy region, and (ii) no assumptions are required for the nuclear break-up in the first incident nucleus-air nucleus collision. A similar conclusion is also reached from a comparison of the GRAPES-3 energy spectra with the direct measurements for the other four nuclear groups. It is seen from Fig. 25 that there is no significant difference in the energy spectra of the He nuclei for these two generators. However, the differences between them widen for the nitrogen and other heavier nuclei.

Among the three direct measurements, JACEE, RUNJOB and SOKOL, the GRAPES-3 results agree rather well with the JACEE and the SOKOL spectra. There is a substantial discrepancy in the flux values of the He nuclei reported by the RUNJOB and the JACEE/ SOKOL experiments. The GRAPES-3 results provide good support and continuity with the measurements from the JACEE and the SOKOL experiments. Another compelling result from the comparisons shown in Fig. 25, relates to the difference in the steepness of the H spectrum relative to the spectra of the other nuclear groups which are decidedly flatter up to ~ 1000 TeV. This difference in the slopes of the energy spectra may have important implications for the nature of the cosmic ray sources and the environment surrounding them and the processes responsible for accelerating the nuclei in the energy range, 100-1000 TeV within the galaxy.

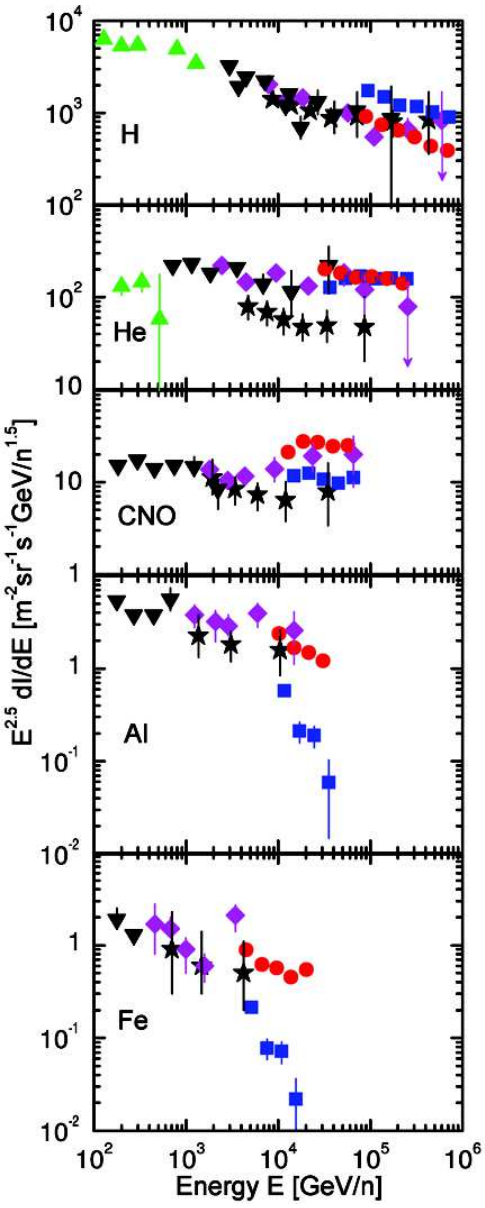

Fig. 25: H, He, CNO, Al, Fe spectra from direct measurements green ▲ Ryan [80], ▼ SOKOL [81], magenta ◆ JACEE [84], ✶ RUNJOB [85], and GRAPES-3 red ● SIBYLL, blue ■ QGSJET

It is also relevant to remark here that the GRAPES-3, proton spectrum agrees very well with the results reported by the other indirect experiments, such as the HEGRA experiment at La Palma [97] and the Tibet AS/γ experiment at Yangbajing [8]. Our results also agree with the KASKADE results [11] on the proton flux at 1000 TeV. However, the results from the Tibet AS/γ experiment are in serious disagreement, both with the GRAPES-3 as well as with the JACEE and the SOKOL results for the He nuclei, probably showing the inadequacy of the shower size spectrum determined with an air shower array alone, to provide the spectral information on the He and other heavier nuclear groups.

The observations of the MMDs with the large GRAPES-3 muon detector have provided convincing evidence for a steeper energy spectrum for the protons, consistent with the results from the direct measurements obtained from the balloon and the satellite borne detectors. The GRAPES-3 results on the energy spectra of He, N, Al and Fe groups also agree well with the direct measurements, extending the energy reach and confirming the flatter nature of the spectra of these nuclei as compared to the protons. The GRAPES-3 results indicate SIBYLL to be a suitable generator for the description of the hadronic interactions in the overlap energy region from 100 to 300 TeV. The extension of the energy spectra by a factor of ~ 3 up to ~ 1000 TeV for the five nuclear groups is also fully consistent with an extrapolation of the spectra measured by the direct methods. With greater confidence in the suitability of the SIBYLL generator at these energies, the analysis of the larger size ($N_e > 10^{5.4}$) showers is now in progress for extending these measurements to the *knee* region and beyond, which may help in understanding the physical process (es) responsible for this critically important feature in the energy spectrum of the primary cosmic rays.

4. Diffuse γ-Ray Limits

There is a direct and intimate connection between the highest energy cosmic rays and the ultra-high energy (UHE, ~ 100 TeV) γ-rays. In principle, this connection may be exploited for an indirect study of the highest energy cosmic rays. Above the GZK cutoff around 4 x 10^{19} eV, the protons have a relatively short path-length before suffering photo-nuclear reactions with the photons of the 2.7°K universal cosmic microwave background radiation, the relic of the big bang. The produced pions and other mesons decay into the electron, the photons and the neutrinos. The Bethe-Heitler pair production in this photon field is another mechanism for the production of γ-rays. Since the electromagnetic decay products, namely, the photons and the electrons also have a relatively short path-length in the photon field of the cosmic microwave background radiation, electromagnetic showers develop in the universe as a consequence of the presence of the cosmic ray particles above the GZK cutoff. The observation of the UHE γ-rays that are the final outcome of the energy loss processes of the extremely high energy cosmic rays in the 2.7°K background [22, 23] becomes an interesting probe of this mechanism. Extensive calculation have shown that the flux of 10-100 TeV γ-rays is within the reach of the planned γ-ray telescopes

There are a number of possible candidate sources for the production of the diffuse flux of UHE ã-rays. Some of the *conventional* scenarios for the production of these γ-rays include; (i) the unresolved point sources, such as the distant active galactic nuclei (AGNs) and the powerful radio galaxies etc., which in addition may also be the sources of the extremely high energy cosmic rays, (ii) the decay of the mesons produced in the collisions of the charged cosmic rays with the interstellar and/or the intergalactic gas and dust, and finally (iii) the electromagnetic showers generated in the interactions of the extremely high energy cosmic rays with the cosmic microwave background photons.

In addition to the *conventional* sources, several *unconventional* astrophysical phenomena have been proposed that could produce a diffuse γ ray flux at the UHE energies. For instance, it has been speculated that the highest energy cosmic rays may not be produced by any acceleration mechanism, but could be the decay product of some super-massive particles (generally termed the X particle) with mass $m_X > 10^{11}$ GeV that can have energies up to ~ m_X. Therefore, no acceleration mechanism is invoked to explain the

highest energy particles. The massive X particles may have originated in the high energy processes in the early universe. Such an *unconventional* non-acceleration, "top-down" decay mechanism as opposed to the *conventional* "bottom-up" acceleration mechanism has significantly different predictions that may be experimentally verifiable [13].

Here we report our attempt to detect the diffuse γ-ray flux above 20 TeV. In the following discussion the physical basis for the criteria utilized in segregating the γ-rays from the proton induced showers is outlined, along with a brief outline of earlier attempts in the same direction. The comparison of the γ-ray with the proton induced showers, based on their muon content provides a rather conservative upper limit on the ratio of the γs to cosmic rays. This is primarily because the showers initiated by the heavier primary cosmic ray nuclei contain significantly larger muon content than the proton initiated showers as described in the previous section. As already described the GRAPES-3 is a large EAS array that was designed for the detailed studies of a number of topics, including the diffuse γ-ray emission around 100 TeV region. The array contains two principle components, namely, the density detectors and the muon detectors that may be seen in Fig. 2.

The UHE γ-rays and protons arriving at the Earth interact in the atmosphere and initiate EAS. The EAS arrays on ground sample the secondary shower particles including the electrons, the photons, and the muons that are produced after several generations of interactions. It is well known that in showers initiated by the cosmic ray nuclei the dominant source of the muons, is decays of the charged mesons produced in the hadronic interactions. However, the γ-ray induced showers being electromagnetic in nature, the cross section for the photo-production of the mesons is much smaller than the pair production, by a large factor of ~ 1000 [101, 102]. As a consequence, we expect a very tiny fraction of the secondary hadrons to be present in the γ-ray induced showers relative to the proton induced showers. Therefore, a drastically reduced number of muons would be present in a γ-ray shower [31].

Extensive Monte Carlo simulations of the EAS have indicated that the γ-ray showers contain a muon content of about a few percent of that found in the showers initiated by the cosmic ray protons of same primary energy. These results on the muon content are based on the conventional values of the electromagnetic and the photo-production cross sections [71, 103]. In the past there have been some reports indicating anomalously high muon content in the γ-ray signals reported from the binary X-ray sources such as the Cygnus X-3 and Hercules X-1 etc. [104-106]. However, the possibility of such an anomalously high cross section for the photo-production of the pions is already ruled out by the H1 [101] and the ZEUS [102] experiments on the electron-proton collisions at the HERA accelerator up to an equivalent laboratory energy of 20 TeV. The pion photo-production cross sections used in the Monte Carlo simulations mentioned above, were based on the HERA measurements and at higher energies they were obtained by a smooth extrapolation of the HERA results.

Since the flux of the cosmic rays reduces rapidly with the primary energy, therefore, a direct and statistically significant measurement of the energy spectrum and the nuclear composition of the primary cosmic rays above 100 TeV can not be performed from the balloon or the space borne platforms. The only practical option available is the indirect method of the detection of the showers produced in the atmosphere, through a ground based array of detectors, where exposure factors of ~ 10^7 m^2h are readily achieved. Since the showers on the surface of the Earth are dominated by the secondary electromagnetic particles that are several generations removed from the primary cosmic ray particle, there is little difference between the showers initiated by primary cosmic ray protons and γ-rays.

The idea of using the muon content of a shower to identify the nature of its primary particle dates back to the sixties. The presence of the muon-poor showers was reported by the BASJE [107-109] and also by a Polish-French [110, 111] collaborations. Subsequently, other detections were also reported by the [112] and the Tien-Shan [113] experiments. The

CASA-MIA collaboration had reported an upper limit on the diffuse flux of UHE γ-rays [114]. Upper limits on the diffuse flux UHE γ-rays was also reported by the HEGRA collaboration in the energy region 65-200 TeV, based on their study of the lateral distribution of the Cerenkov photons in the EAS [28]. The EASTOP collaboration had also probed the diffuse UHE γ-rays above 870 TeV using the muon-poor criterion [30]. The CASA-MIA collaboration had subsequently reported newer and more stringent upper limit with their complete detector system between 570 TeV and 5.5 PeV based on the muon content of the EAS [31]. The segregation of the γ-ray from the proton induced showers has become a reality, with the advent of the large area muon detectors that are operated in association with EAS arrays, which have permitted the detection of the muons with good statistics.

As mentioned earlier, the γ-ray initiated showers contain far fewer (< 5%) muons as compared to the proton initiated showers. Therefore, the criterion of the showers being unaccompanied by the muons, the so called μ-poor showers, provides an efficient identification of the γ-ray initiated showers. This hypothesis is strongly backed by the results obtained from detailed Monte Carlo simulations that have been carried out by several independent groups in recent times [30, 31, 115]. A total of 5.9 x 10^8 showers collected over a total live time of 4.5 x 10^7 s (525 d), spread over the 2-year period from March 2000 to December 2001, were analyzed for determining various shower parameters, namely, the arrival direction, defined by the zenith (θ) and the azimuthal (ϕ) angles, the shower size (N_e), the core position (x_c,y_c) and the shower age (s). For each shower, the zenith angle θ and the azimuthal angle ϕ were determined by using the timing information from the TDC information for each detector by fitting a conical shower front. The angular resolution of the GRAPES-3 EAS array was estimated by using three different methods, namely, the even-odd, the left-right as well as from the observation of the shadow of the Moon on the isotropic flux of the cosmic rays. The angular resolution was estimated to be 0.7^o for the showers of energy as low as 30 TeV [76].

For the selection of the showers, the following cuts were imposed during the off-line analysis; (a) out of the four scintillator detectors with the largest particle densities recorded, the outer-most ring of the detectors must not contribute more than one detector, (b) the sum of the number of particles in the four detectors with the highest density must be ≥ 10, (c) for the six detectors with the highest density, the distance from the center of the array should not exceed 30 m, (d) number of particles detected in the outermost two rings should not exceed 35 % of the total number of particles detected by the array.

For the analysis of the muon component the detected muon number was estimated from the observed muon tracks in the four layers of the detector. Further, the direction of each muon was required to match within 10^0 with the arrival direction of the shower determined from the electromagnetic component. The number of the detected muons depends on the primary energy of the EAS, the distance of the shower core from the muon detector, and the area of the muon detector. In the GRAPES-3 EAS array, typically several muons are detected if the total number of detected particles in the density detectors exceeds 30, for the distances of the muon detector to the EAS core of ≤ 30 m. The width of the gate for the recording of the muons was 5 μs. The muon count rate, unrelated to the EAS trigger was ~ 4000 s^{-1} per module for the muon that generate a coincidence in any 3 out of the 4 layers. Therefore, a conservative estimate of the mean number of muons due to accidental coincidences is 0.23 per EAS for all four supermodules in the muon detector. This rate drops to 0.07 per EAS after the condition of the alignment of the muon and EAS directions is imposed. In Fig. 4 we show the muon multiplicity distributions for different shower size groups as classified by the detected number of particles in an EAS.

As already mentioned, the γ-ray induced showers are muon-poor as compared to the proton induced showers due to the production of a minuscule number of secondary hadrons through the photo-production processes. The Monte Carlo simulations carried out using the CORSIKA code show that about

2-3% of muons are expected from the γ-ray as compared to the proton induced shower of the same primary energy. Since the typical events recorded by the GRAPES-3 array contain zero to several tens of muons, we have classified the showers with no associated muons as the muon-poor events. The upper limit on the ratio of the γ-rays to the cosmic rays was obtained using the muon-poor criterion for the selection of the γ-ray candidates as is described below. The real challenge was to design the selection cuts for the proton induced showers that ensured the detection of a finite number of muons.

First, we calculated the median value of the energy of the primary cosmic rays from the distribution simulated using CORSIKA for a given value of the detected particle density. In the energy range from ten to a few hundred TeV, we did not find any significant difference between the proton and the γ-ray primaries. This simulation provided the number of muons for each shower, allowing the probability of the detection of muon-poor γ-ray showers to be estimated as a function of the distance from the center of the muon detector. Therefore, the same selection criteria was applied for the density detectors for both the γ-ray and proton showers. Next, we use the cosmic ray energy spectrum and constrain the core position in the simulations to generate the γ-ray induced showers including the trigger effects and the errors in the estimation of the core position etc. Using these results, we calculated the efficiency for the detection of the γ-ray induced showers as muon-poor events. The observational data and the simulation results are displayed in the table. The upper limit on the ratio of γ-to proton flux is given by

$$\frac{I_\gamma}{I_{CR}} = \frac{N_{\mu-poor}(90\%C.L.)}{N_{all}} \frac{1}{\varepsilon_\gamma} \left(\frac{E_{CR}}{E_\gamma} \right)^{-\alpha} \qquad (13)$$

where $N_{\mu\text{-poor}}$ (90 % C.L.) is the 90 % confidence level upper limit on the number of muon-poor air showers assuming a Poisson distribution, N_{all} is the total number of air showers, ε_γ is the efficiency for the detection of the γ-ray induced air showers as muon-poor air showers. E_{CR} is the median cosmic ray energy and E_γ is the median γ-ray energy and α (=2.65) is the power-law spectral index of the primary energy

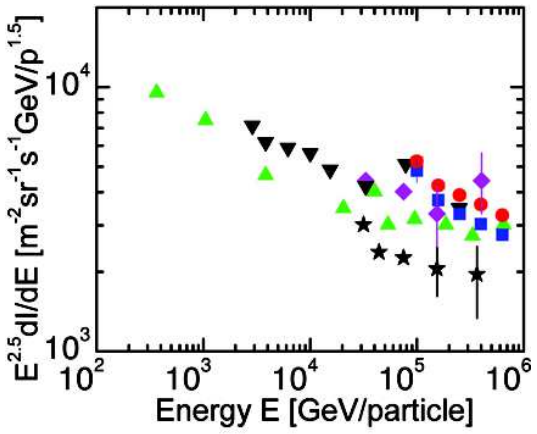

Fig. 26: All-particle spectra from direct measurements ▲ Grigorov [82], ▼ SOKOL [81], magenta ◆ JACEE [84], ✶ RUNJOB [85], and GRAPES-3 red ● SIBYLL, blue ■ QGSJET

spectrum.

The upper limits obtained from the GRAPES-3 experiment are shown in Fig. 27 and are compared with the results published by other groups. It is seen that the GRAPES-3 upper limits on the ratio I_γ/I_{CR} from the present work are comparable to the ones placed by the HEGRA group [29] for the 50-100 TeV region. However in the 100-550 TeV region, the

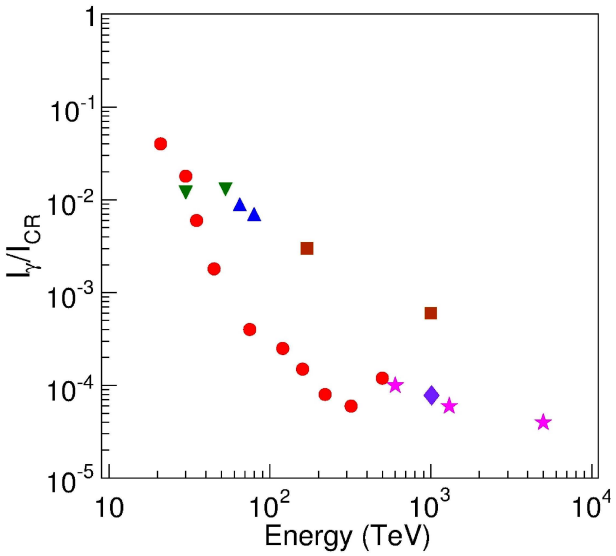

Fig. 27: Upper limit on the ratio of γ-rays to protons as a function of primary energy for, (a) HEGRA green ▼ [27], (b) AIROBICC blue ▲ [26], (c) UTAH-MICHIGAN yellow ■ [95], (d) EASTOP purple ◆ [28], (e) CASA-MIA magenta ✶ [29], (f) GRAPES-3 present work red ●

GRAPES-3 upper limits are significantly more sensitive than the ones placed by the AIROBICC [28], Utah-Michigan [114], EASTOP [30], and CASA-MIA [31] experiments. In the important 50-200 TeV energy region the GRAPES-3 upper limits are about an order of magnitude smaller than the rest. The limit of 10^{-4} on the ratio I_γ/I_{CR} at 200 TeV rules out models based on topological defects for the production of highest energy cosmic rays.

5. Solar Phenomena

5.1 High Energy Protons in Solar Flares

The GRAPES-3 muon detector is uniquely suited for studies of solar flares, coronal mass ejections and these studies provide valuable information on the space weather. Solar flares accelerate charged particles through a variety of mechanisms, which may be constrained through observations at high energies (> 10 GeV). We have searched for direct emission of protons of energy ≥ 20 GeV in association with an X17 class solar flare that occurred on 28 October 2003, using the large area tracking muon telescope of the GRAPES-3 experiment at Ooty. A 99 % C.L. upper limit on the flux of protons due to the solar flare was placed at 1.4 x 10^{-6} $cm^{-2}s^{-1}sr^{-1}$. A separate upper limit on the narrow solid angle flux of protons at 4 x 10^{-6} $cm^{-2}s^{-1}sr^{-1}$ was also placed. Solar flares are also associated with coronal mass ejections, which propagate through the interplanetary space producing geomagnetic storms and Forbush decrease (Fd) events, upon their arrival at the Earth. New information on the structure and time evolution of the large Fd observed on 29 October 2003 by GRAPES-3 is also presented here. The onset of Fd in nine different solid angle bins (~ 0.3 sr) shows a remarkably similar behavior, with an evolution on a time scale of ~ 1 h. A power law dependence of the magnitude of the Fd on the cutoff rigidity was derived, using the data from tracking muon telescope, over a narrow range of cutoff rigidity 14.3-24.0 GV, which showed a spectral slope "$\gamma = 0.53 \pm 0.04$", in agreement with earlier measurements.

The very large area tracking muon telescope operating as part of the GRAPES-3 experiment [60, 61] is an unique instrument used to search for the high energy protons emitted during the active phase of a solar flare. The muon telescope is capable of providing a high statistics, directional study of muons. The GRAPES-3 muon telescope has a total area of 560 m^2, consisting of 16 modules, each of which is 35 m^2 in area. These modules are located very close to each other as shown in Fig. 2. A cluster of four 35 m^2 area neighboring modules, located inside a common hall, constitutes one supermodule with a total area of 140 m^2. The energy threshold of the telescope is 1GeV for the muons arriving along the vertical direction. The cutoff rigidity at Ooty is 17 GV in the vertical direction and varies from 12 to 42 GV across the field of view of the tracking muon telescope The percent variation observed in the muon rates from a single module is consistent with a statistical error of 0.04 %, expected from the total muon counts ~ 6 x10^6 over a period of 30 min in the sample. This high level of precision permitted a very detailed study of the cosmic ray intensity variation to be carried out. For example, the onset of the Forbush decrease on 29 October 2003 which started ~ 20 h after the start of an X17 class solar flare at 09:51 UTC on 28 October 2003 was studied in considerable detail with the GRAPES-3 instrument.

However, most of the detected muons are generated by ≥ 20 GeV galactic cosmic rays, which are of little interest to us here, except for the fact that they form a stable and dominant background to the variation in the muon flux produced by the solar flare. The statistical variations in the muon rate are relatively small in magnitude because of the large area of the GRAPES-3 muon telescope, as ~ 3 x 10^6 muons are detected every minute, from the hits recorded in the 3712 PRCs of the GRAPES-3 muon telescope [61]. The muon data are grouped online every 10 s, into solid angle bins of ~ 0.05 sr, consistent with the angular resolution of the muon telescope. However, despite the drastic reduction in the data generated due to this angular segmentation, we still record ~ 9 GB of data from the four supermodules every day.

The relativistic solar particles can provide a key to the understanding of the acceleration processes at work in the Sun. The global network of NMs has

been used to detect relativistic neutrons produced in the atmosphere from the interactions of the high energy particles from the Sun, which were accelerated during the solar flare on 28 October 2003 around 11:10 UTC nearly 80 min after the detection of this flare in x rays. This solar flare had followed in the wake of the highly disturbed interplanetary conditions prevailing because of the earlier eruptions that had occurred in the Sun. We have searched for the direct emission of protons at the time of this solar flare. However, during the period of interest only three out of four supermodules were operating and therefore the total area of the muon detector was reduced to 420 m^2. In Fig. 28 the pressure-corrected GRAPES-3 data of 28 October 2003 for the muon rates summed over the three working supermodules is displayed. The variation in the rate of muons, with an amplitude of ~1 % due to the diurnal anisotropy is clearly visible. However, no statistically significant excess was recorded in the time interval of 30 min after the start of the solar flare at 09:51h UTC, indicated by the first arrow in Fig. 28 or after 11:10 h UTC, indicated by the second arrow when the global network of NMs started recording an increase in the rate of neutrons.

The value of 30 min was selected as the energetic (multi-GeV) protons are expected to arrive within 1-2 times the light travel time (8-16 min) from the Sun to the Earth as given in the model quoted above [116]. However, in the absence of the precise knowledge of the energy spectrum of solar protons at high energy and that of the interplanetary magnetic field, there is a considerable degree of uncertainty in the actual travel time of the energetic solar protons. The NM data showed the presence of the proton flux over an extended period of time. Thus an interval of 30 min was expected to provide a reasonable time window for the detection of any direct high energy protons from the solar flare. The exact choice of the time window is not a critical parameter because the upper limit on the proton flux is not particularly sensitive to the duration of the time window selected. Since > 1 GeV muons are secondaries produced by the primary protons of energy ≥ 20 GeV in the atmosphere, therefore these observations were used to place a 99 % C.L. upper limit of 1.4 x 10^{-6} $cm^{-2}s^{-1}$ sr^{-1} on the wide-angle (~ 2.5 sr) flux of solar protons. The tracking muon telescope is being operated round the clock to search for direct protons during the solar flares which may occur in the future.

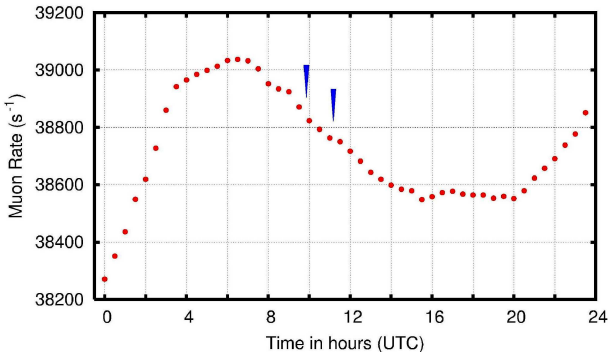

Fig. 28: Variation in total muon rate for 3 supermodules on 28 October 2003, after atmospheric pressure correction. Start of solar flare indicated by the first arrow. Second arrow indicates start of prompt component detected by NMs

It is well known that the solar protons of energies of tens of GeV, need not be observed from the direction of the Sun, due to their deflection in the interplanetary and geomagnetic fields. Therefore, it is possible to enhance the sensitivity of the muon detector by incorporating the measurement of the arrival direction of the muons. This novel feature was incorporated into all four supermodules of the GRAPES-3 detector by recording the muon direction into 225 solid angle bins. This capability was achieved after the installation of new, additional direction-sensitive trigger electronics and a separate data acquisition system for each of the four supermodules. As shown in Fig. 29, for each PRC in the lower layer, the muon angle is determined and binned into 15 angular bins based on the specific PRC triggered in the upper layer from among the 15 PRCs, one directly above (central PRC) and 7 each on either side of the central PRC. This angular binning is carried out in each of the two orthogonal projections (XZ and YZ), thereby generating a 2-dimensional 15 x 15 = 225 solid angle map of the muon directions. The contents of the 225 solid angle bins are recorded, once every 10s, thus permitting a continuous monitoring of the directional flux of the muons in the sky.

Although the excess in the muon rate can be

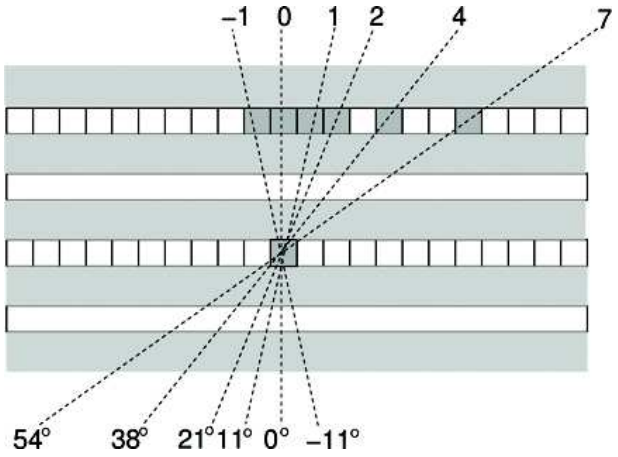

Fig. 29: A schematic view of muon arrival angle selection based on the PRC triggered in the lower and 15 PRCs directly above, in the upper layer. Triggered PRCs are shown as filled squares

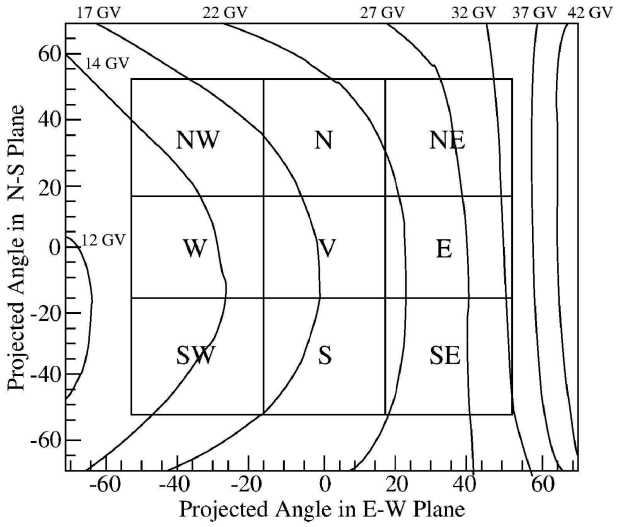

Fig. 30: A schematic of nine solid angle bins of muon arrival directions. Also shown are contours of constant geomagnetic cutoff rigidity in the field of view. The cutoff rigidity varies from 12 to 42 GV in the FOV of GRAPES-3 muon telescope

searched for in any of the 225 solid angle bins, it is expected that the flux of the solar protons from a flare would be spread over several bins. This directional spread could arise from a number of factors, namely, (a) the size of the bin is comparable to the angular resolution of the muon telescope, (b) the magnetic field in the solar flare and in the interplanetary regions, (c) the terrestrial magnetic field, and (d) the transverse momentum imparted in the atmospheric collisions. Therefore, for the purposes of the present study, the muons have been regrouped into 3x3 = 9 coarse solid angle bins, as shown schematically in Fig. 30. This regrouping of the data has been done by either combining a set of 3x5 or 5x5 solid angle bins. The exception being the vertical direction which combines 3x3 bins. This peculiar choice of binning is dictated by the fact that the muon flux is comparatively larger for the near central directions (N, E, W, S) as compared to the outer directions (NE, SE, NW, SW). This regrouping of the data results in a relatively similar solid angle coverage for the nine bins. Therefore, this re-binning also results in muon statistics for various bins which are not too dissimilar from each other. The geomagnetic cutoff rigidity for the field of view (FOV) of the GRAPES-3 muon telescope varies significantly for the nine solid angle bins. In Fig. 30 the contours of the constant geomagnetic cutoff rigidity in the FOV are superimposed over the schematic of the nine solid angle bins of the muon arrival directions in two orthogonal projected planes. The geomagnetic cutoff rigidity varies from a low value of 12 GV in the west to 42 GV in the east direction within the FOV of the GRAPES-3 tracking muon telescope. Thus the measurement of the direction of muons in the GRAPES-3 experiment permits the effect of the rigidity on various solar phenomena to be systematically studied.

No statistically significant excess was seen, from any of the nine directions in the muon rate, during an interval of 30 min, after the start of the solar flare at 09:51 h UTC on 28 October 2003. A 99 % C.L. upper limit of 4×10^{-6} $cm^{-2}s^{-1}sr^{-1}$ on the narrow-angle (~ 0.3 sr) flux of the solar protons of $\geq$ 20 GeV from each of the nine angular regions was placed. The GRAPES-3 wide-angle upper limit along with those obtained for the solar flares of 29 September 1989 by the Baksan group [49] and of 14 July 2000 by the L3 [52] are also shown in Fig. 31. A flux of neutron of 2×10^{-4} $cm^{-2}s^{-1}$ above 10 GeV claimed by the AGASA group [51] for the solar flare of 4 June 1991 is also shown in Fig. 31. For a comparison the flux of particles recorded using NMs during one of the largest flares recorded on 23 February 1956 and the one on 15 April 2001 is also

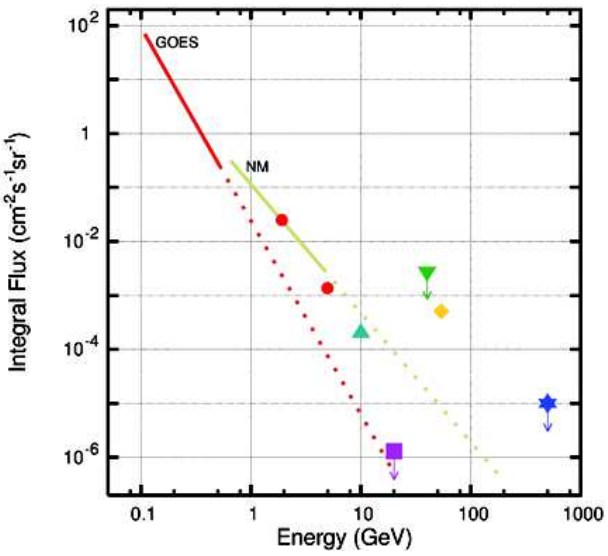

Fig. 31: Integral flux of protons with energy on 28 October 2003; (a) based on 100-600 MeV GOES-10/11 and sub-GeV balloon data, (b) worldwide NM data, (c) magenta ■ ≥ 20 GeV GRAPES-3 upper limit, (d) green ▲ > 10 GeV AGASA flux on 4 June 1991, (e) green ▼ > 40 GeV L3 upper limit on 14 July 2000, (f) blue ✶ > 500 GeV Baksan upper limit on 29 September 1989, (g) red ● NM data on 15 April 2001, (h) yellow ◆ NM data on 23 February 1956

shown in Fig. 31. The flux of the solar neutrons for the 4 June 1991 flare was estimated to be 1-2 x 10^{-4} $cm^{-2}s^{-1}$ which is about two orders of magnitude larger than the 99 % C.L. upper limit of 1.4 x 10^{-6} $cm^{-2}s^{-1}sr^{-1}$ on the wide-angle flux of particles placed by GRAPES-3 for the 28 October 2003 flare. In addition, the tracking feature of GRAPES-3 muon telescope allowed us to place a slightly less stringent 99 % C.L. upper limit of 4 x10^{-6} $cm^{-2}s^{-1}sr^{-1}$ on the narrow-angle flux of solar flare particles, for which, in absence of tracking, there is no counterpart in the AGASA experiment.

Based on the past observations, the energy spectra of the particles accelerated in the solar flares display considerable complexity. It is reasonable to assume that the energy spectrum of the particles accelerated during a solar flare follow a power law. A compilation of the major solar flare events during the past 60 yr has shown that the spectral index of the assumed power law shows progressive steepening with increasing energy of protons, reaching a value of 3.5-4.0 at energies above 10 GeV [117]. However, it is very difficult to arrive at a definitive conclusion on the energy spectrum of the solar flare particles in view of the huge variation seen from flare to flare; based on the past claims, it is likely that the solar flares may accelerate protons to energies well above 100 GeV [45, 49]. A lower limit on the spectral index of an assumed power law for the energy spectrum of the 28 October 2003 flare can be placed at $\gamma \sim 5.3$ based only on the worldwide NM and the GRAPES-3 data. However, in view of the rapidly changing spectral indices and/or cutoffs observed in the case of most of the solar flares, the actual value of the spectral index is likely to be significantly higher [117]. The narrow-angle upper limits on the flux of solar flare particles derived for the nine bins are very similar and for that reason a common value of 4 x 10^{-6} $cm^{-2}s^{-1}sr^{-1}$ is obtained.

5.2 Forbush Decrease

In addition to the acceleration of particles due to the energy released from the coronal loops, the solar flares are also associated with the coronal mass ejections which are blobs of plasma ejected during the flaring activity. An expanding CME-driven shock front accelerates ions at various helio-longitudes. Apart from the complex structure of a CME and its interaction with the heliospheric magnetic cavity, its effect on the structure of the geomagnetic field is also very important for various studies at the Earth. It is widely recognized that the CMEs and high-speed streams from the coronal holes have considerable influence on the propagation of the particles within the heliosphere. The interaction of these flows with the quiet solar wind creates regions of compressed heated plasma and shocks which are responsible for further acceleration and modulation of the particles incident over the atmosphere of the Earth. Detailed observations on the modulation of the cosmic rays, using NMs and muon telescopes, provide important information for modeling the propagation and acceleration of the solar energetic particles in the interplanetary medium. The short-term modulations such as Fds may be related, either directly to the material ejected from the Sun or to the transient interplanetary shocks generated by these ejections [54, 55].

The capability to observe the directional muon flux, with the three working supermodules, provides a completely new view of the evolution of a Fd, which should help in modeling the propagation of the high energy particles in the interplanetary and in the near-Earth regions. This may be seen from the detailed information available on the Fd, observed on 29 October 2003 from the nine solid angle bins, each with a solid angle coverage of ~ 0.3 sr as displayed in Fig. 30. The observed muon rate for time intervals of 6 min for one of the nine bins, namely, "V", after applying appropriate corrections for the variation in the atmospheric pressure as a function of time in hours UTC on 29 October 2003, is shown in Fig. 32. The rapid onset of the Forbush decrease starting around 7 h and lasting until 18 h UTC is clearly visible. Also shown in Fig. 32 is a dot next to the legend 1 σ whose diameter represents the size of 1 σ error bar. Therefore, the rich structure in the muon rate seen during the onset of Fd is to be regarded as real, and it indicates the rapid variation in the evolution of the Fd on a time scale of minutes. It has been pointed out that a "two-step" structure observed in several Fds is caused by the ejecta and the shock effects of the CME [118]. Therefore, any model proposed to account for the particle acceleration and propagation through the interplanetary space during a solar flare should also be able to explain this rich time structure during the onset phase of the Fd.

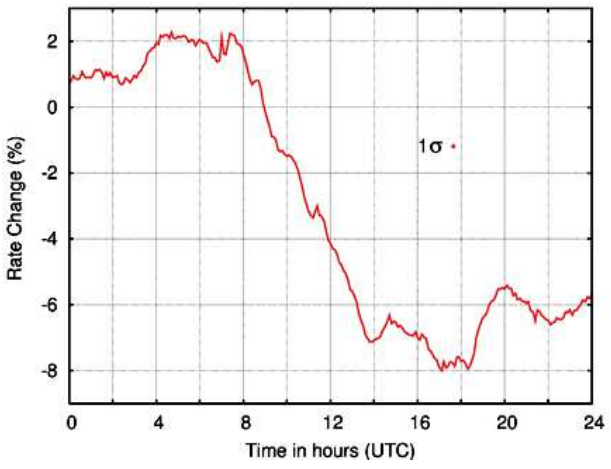

Fig. 32: Observed variation in muon rate on 29 October 2003 in the vertical bin "V". Muon rates shown are for 6 min intervals. Diameter of small dot right of legend 1 σ equals 1 sigma statistical error bar

As shown in Fig. 30, the geomagnetic cutoff rigidity for the nine bins in the GRAPES-3 field of view varies from 14 to 42 GV. This fact combined with the high quality GRAPES-3 muon data, makes it possible to study the rigidity dependence of the magnitude of the Forbush decrease observed on 29 October 2003. The mean geomagnetic cutoff rigidity for the nine solid angle bins varies from 14.3 GV in west to 24.0 GV in the east direction. The muon rates averaged over 6 min successive intervals for the nine solid angle bins were used to estimate the magnitude of the Fd in each direction. In Fig. 33(a) the magnitude of the Fd is shown, as a function of geomagnetic cutoff rigidity for the nine bins. A clear inverse correlation between the geomagnetic cutoff rigidity and the magnitude of Fd can be noticed, because the magnitude of the Fd decreases as the cutoff rigidity increases. A change of 1.6 % in the magnitude of the Fd is seen in going from 14.3 to 24 GV. However, another interesting feature of this variation is the set-wise clustering of the values of the Fd magnitudes into groups of three bins. The three east bins labeled NE, E, SE and represented by filled circles in Fig. 33 (a) form a cluster. But the middle bin "E" shows a sizable departure in its magnitude (~ 0.4 %) as compared to the two outer bins NE and SE. Similarly the three center bins labeled N, V, and S represented by filled triangles also show clustering with bin V separated by ~ 0.5 % from the other two bins N and S. The displacement of bin W in the west set, represented by filled squares, is the largest ~ 0.8 % with respect to the remaining two bins, namely, NW and SW.

The inverse correlation between the magnitude of the Fd and the geomagnetic cutoff rigidity is an established feature of the phenomenon of Fd, and it can be readily understood on the basis of the rigidity spectrum of the modulation of the cosmic rays. The rigidity dependence of the magnitude of the Fds have been measured by a number of groups primarily using NMs. The rigidity dependence can be reasonably approximated by a power law of the type, $K \times r^{-\gamma}$ where r is the rigidity in GV and the measured spectral index γ ranges from 0.4 to 1.2 [118]. Although the observed displacement of the middle bin relative to the remaining two bins in each set is rather small (~

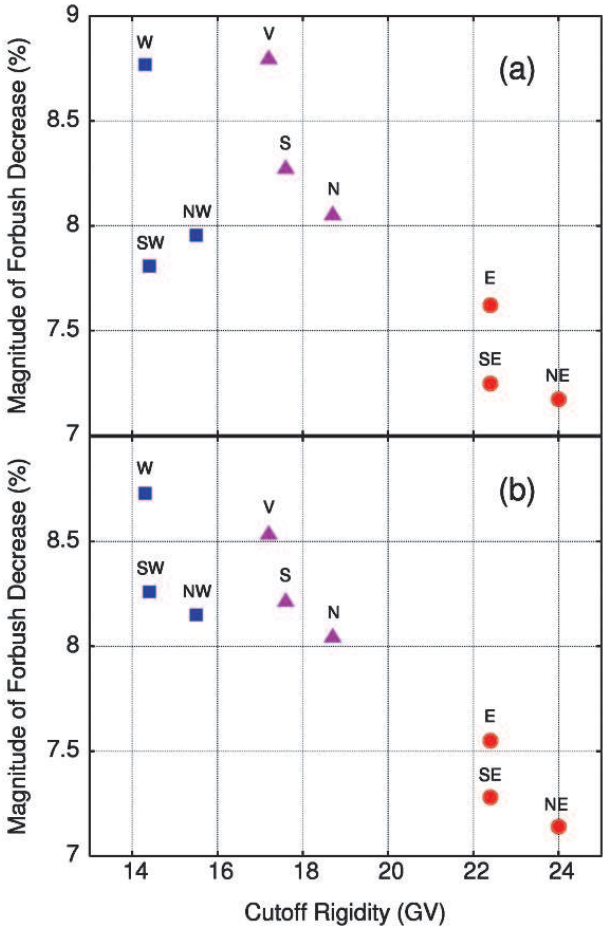

Fig. 33: (a) Observed variation in the magnitude of Forbush decrease (%); (b) Simulations for the magnitude of Forbush decrease (%). Both as a function of geomagnetic cutoff rigidity (GV) for the three sets of nine solid angle bins, namely, (i) NE, E, SE (filled circles), (ii) N, V, S (filled triangles), (iii) NW, W, SW (filled squares). The middle bins (E, V, W) display sizable deviations ~ 0.5 % from the remaining two bins. Simulations are for a rigidity dependence of Fd magnitude = 12.8 % x $(r/30)^{-0.53}$

0.5%), given the small value of the statistical error in our measurements this effect becomes significant. Note that the middle bins (E, V, and W) in the respective sets of solid angle bins point to a direction, closest to the local vertical direction. Therefore, not surprisingly, these three bins record a larger flux of muons due to a lower threshold energy, caused by a relatively smaller angle of incidence. In order to determine the dependence of the magnitude "*A(r)*" of the Fd (in %) in a given bin, Monte Carlo simulations were carried out with an assumed rigidity dependence described by the following power law:

$$A(r) = K(\%) \times (r/30)^{-\gamma} \qquad (14)$$

where *r* is the rigidity in GV. In simulations the effect of the instrumentation such as the rigidity cutoff, solid angle of acceptance, angle of incidence, etc. were included to compute the expected magnitude of the Fd, for the nine bins. A chi-square minimization method yielded the following values for the parameters of the power law fit: $K = (12.8 \pm 0.3)$ % and $\gamma = 0.53 \pm 0.04$. This Monte Carlo simulation gave an rms spread of 0.19 % in the magnitudes of observed and simulated data. A rms value of 0.19 % between observed and simulated data sets, although larger than the intrinsic statistical error in the observed data of ~ 0.1%, this disagreement is not considered unsatisfactory in view of the numerous simplifications made in carrying out the Monte Carlo simulations.

The simulated magnitudes of the Fd for the nine bins are shown in Fig. 33(b). The simulated data reproduces the pattern of Fd magnitudes which is very similar to that of the observed data. The close agreement between Monte Carlo simulations and observations indicates that the major features of the data have been adequately accounted for in terms of known effects such as the angle of incidence, energy threshold, etc. The value of the spectral index $\gamma = 0.53 \pm 0.04$ of the rigidity dependence of the magnitude *A(r)* of the Fd is in agreement with the other measurements (0.4-1.2) as mentioned earlier [118]. Present observations also demonstrate the ability of the GRAPES-3 muon telescope to make precision measurements on the solar phenomenon such as the Forbush decrease, including its rigidity dependence and anisotropy in real time. Finally a search for direct emission of protons of $\geq$ 20 GeV in association with the solar flare of 28 October 2003 yielded a 99 % C.L. upper limit on the wide-angle flux of the solar protons at 1.4 x 10^{-6} cm^{-2} s^{-1} sr^{-1}. This upper limit is significantly lower than the limits and/or fluxes reported by all other experiments at comparable energies. The tracking feature built into the GRAPES-3 muon telescope was exploited to carry out a narrow solid angle search of the direct protons. The negative result obtained was used to place a 99 % C.L. upper limit of 4 x10^{-6} cm^{-2} s^{-1} sr^{-1}. The

significance of this novel feature of the GRAPES-3 muon telescope was discussed in relation to the observations pertaining to the propagation of the solar flare particles in the interplanetary medium near the Earth. New information on the time evolution during the onset of the Forbush decrease of 29 October 2003, on a time scale of an hour, is provided. Rigidity dependence of the magnitude of the Fd, over a relatively narrow range of geomagnetic cutoff rigidity (14.3-24.0 GV) was derived using the data from the tracking muon telescope. The estimated value of the spectral index $\gamma = 0.53 \pm 0.04$ is in agreement with the earlier measurements which range from 0.4 to 1.2.

6. Future Plans

Expansion plans in a number of areas including doubling of the area of the muon detector is being initiated to further increase the sensitivity of this experiment. Plans are also afoot to install a large imaging telescope to measure the Cerenkov component of the EAS in a bid to expand the reach of the experiment to include this component which would provide information on the longitudinal development of the EAS and also the primary energy in a completely independent manner. It is also proposed to expand the area of the array with reduced detector density to cover a much larger area to extend the energy reach of the experiment to 10^{18} eV and thereby create a single facility to study the cosmic radiation all the way from 10^{13} to 10^{18} eV, a range of nearly 5 orders of magnitude. Finally plans are underway to install neutron monitors to further enhance the capability to study various space weather phenomena.

7. Summary

A brief survey of the present GRAPES-3 experiment, after starting from the early activity in the fifties has been presented. Continuing with the philosophy of Acharya J.C. Bose and Dr. Homi J. Bhabha with strong emphasis on the development of state-of-the-art detectors and signal processing electronics has in the long run paid rich dividends. Allowing the GRAPES-3 collaboration to perform world-class experiments in astroparticle physics at a fraction of the cost elsewhere. The thriving activity has attracted a large number (34) of scientists from within India and abroad to join and contribute to further growth of this activity. The GRAPES-3 collaboration has demonstrated its unique capability to measure the cosmic ray composition with unprecedented resolution. The GRAPES-3 collaboration has also placed the most sensitive upper limits on the diffuse flux of 100 TeV γ-rays and is now poised to make still more sensitive measurements with the planned expansion of this experiment. Precision studies of the Sun induced phenomena such as the solar flares, coronal mass ejections are offering a new probe to study the space weather.

Acknowledgment

I am grateful to every present and past member of the GRAPES-3 collaboration stationed in Ooty, Mumbai, Osaka and elsewhere for making this experiment possible, and for carrying out the research and developmental activities that were summarized here. These multi-tasking members of the GRAPES-3 collaboration have made indispensable contributions to the success of this enterprise and their energy has made it a joy for me to work with them. I thank Pranaba Nayak for assisting in converting the original document written in *LaTex* to word format required for PINSA as well as for pointing out several mistakes in the manuscript. Special thanks are due to Sibaji Raha for extending the invitation to write this article and encouraging me all the way.

References

1. Bose JC (2009) Inaugural address in dedication of the Bose Institute, November 30, 1917. *Phys News* **39** 20-26
2. Sreekantan BV (1998) The cosmic ray story. *NIAS Report* R4-98
3. Bhat PN *et al.* (1982) Delayed energetic events in extensive air showers. *Phys Rev D* **25** 2820-2838. doi: http://dx.doi.org/10.1103/PhysRevD.25.2820
4. Gupta SK *et al.* (1985) A design study of atmospheric Cerenkov radiation telescope for very high energy gamma-

ray astronomy. *Astrophys Space Sci* **115** 163-183. doi: 10.1007/BF00653836

5. Kobayakawa K *et al*. (2002) Acceleration by oblique shocks at supernova remnants and cosmic ray spectra around the knee region, *Phys Rev D* 66 (2002) 083004. doi: http://dx.doi.org/ 10.1103/PhysRevD.66.083004
6. Glasmacher MAK *et al.* (1999) The cosmic ray energy spectrum between 10^{14} and 10^{16} eV. *Astropart Phys* **10** 291-302. doi: 10.1016/S0927-6505(98)00070-X
7. Aglietta M *et al*. (1999) The EAS size spectrum and the cosmic ray energy spectrum in the region 10^{15}–10^{16} eV. *Astropart Phys* **10** 1-9. doi: 10.1016/S0927-6505(98)00035-8
8. Amenomori M *et al*. (2000) Primary proton spectrum between 200 TeV and 1000 TeV observed with the Tibet burst detector and air shower array. *Phys Rev D* **62** 112002. doi: http://dx.doi.org/10.1103/PhysRevD.62.112002
9. Bassi C *et al*. (2000) High altitude test of RPCs for the Argo YBJ experiment. *Nucl Instr Methods A* **443** 342-350. doi:10.1016/S0168-9002(99)01079-7
10. Gupta SK *et al*. (2003) Observations on muon multiplicity distribution with the GRAPES-2 experiment at Ooty for studies on the mass composition of cosmic rays at PeV energies. *Phys Rev D* **68** 052005. doi: http://dx.doi.org/ 10.1103/PhysRevD.68.052005
11. Antoni T *et al*. (2005) KASCADE measurements of energy spectra for elemental groups of cosmic rays: Results and open problems. *Astropart Phys* **24** 1-25. doi: 10.1016/ j.astropartphys. 2005.04.001
12. Watson AA (2000) Ultra-high-energy cosmic rays: the experimental situation. *Phys Rep* **333-334** 309-327. 10.1016/S0370-1573(00)00027-2
13. Bhattacharjee P and Sigl G (2000) Origin and propagation of extremely high-energy cosmic rays. *Phys Rep* **327** 109. doi: 10.1016/S0370-1573(99)00101-5
14. Bird DJ *et al*. (1993) Evidence for correlated changes in the spectrum and composition of cosmic rays at extremely high energies. *Phys Rev Lett* **71** 3401-3404. doi: http:// dx.doi.org/10.1103/PhysRevLett.71.3401
15. Hayashida N *et al*. (1994) Observation of a Very Energetic Cosmic Ray Well Beyond the Predicted 2.7 K Cutoff in the Primary Energy Spectrum, *Phys Rev Lett* **73** 3491-3494. doi: http://dx.doi.org/10.1103/PhysRevLett.73.3491
16. Abraham J *et al*. Properties and performance of the prototype instrument for the Pierre Auger Observatory (2004) *Nucl Instr Methods A* **523** 50-95. doi: 10.1016/ j.nima.2003.12.012
17. Fukushima M *et al*. (2007) Proc. 30th International Cosmic Ray Conference (Merida) **4** 417
18. Greisen K (1966) End to the Cosmic-Ray Spectrum? *Phys Rev Lett* **16** 748-750. doi: http://dx.doi.org/10.1103/ PhysRevLett.16.748
19. Zatsepin GT and Kuzmin VA (1966) Upper limit of the spectrum of cosmic rays. *JETP Lett* **4** 78-80
20. Abraham J *et al*. (2008) Observation of the Suppression of the Flux of Cosmic Rays above $4x10^{19}$eV. *Phys Rev Lett* **101** 061101-1-7. doi: http://dx.doi.org/10.1103/ PhysRevLett.101. 061101
21. Bluementhal GR (1970) Energy Loss of High-Energy Cosmic Rays in Pair-Producing Collisions with Ambient Photons. *Phys Rev D* **1** 1596-1602. doi: http://dx.doi.org/ 10.1103/PhysRevD.1.1596
22. Wdowczyk J, Tkaczyk W and Wolfendale AW (1972) Primary cosmic γ-rays above 10^{12} eV. *J Phys A* **5** 1419-1432. doi:10.1088/0305-4470/5/9/015
23. Stecker FW (1973) Ultrahigh energy photons, electrons, and neutrinos, the microwave background, and the universal cosmic-ray hypothesis. *Astrophys Space Sci* **20** 47-57. doi: 10.1007/BF00645585
24. Berezinskii VS and Kudryavtsev VA (1988) On the diffuse ultra high energy $E_g > 10^{14}$ eV gamma-ray flux. *Sov Astr Lett* **14** 370
25. Halzen F *et al*. (1990) Cosmology with 100-TeV ã-ray telescopes. *Phys Rev D* **41** 342-346. doi: http://dx.doi.org/ 10.1103/PhysRevD.41.342
26. Vilenkin A (1985) Cosmic strings and domain walls. *Phys Rep* **121** 263-315. doi: 10.1016/0370-1573(85)90033-X
27. Aharonian FA, Bhattacharjee P and Schramm DN (1992) Photon/proton ratio as a diagnostic tool for topological defects as the sources of extremely high-energy cosmic rays. *Phys Rev D* **46** 4188-4192. doi: http://dx.doi.org/ 10.1103/ PhysRevD.46.4188
28. Karle A *et al*. (1995) Search for isotropic ã radiation in the cosmological window between 65 and 200 TeV. *Phys Lett B* **347** 161-170. doi: 10.1016/0370-2693(95)00132-5
29. Aharonian FA *et al*. (2002) Limits on the TeV flux of diffuse gamma rays as measured with the HEGRA air shower array. *Astropart Phys* **17** 459-475. doi: 10.1016/ S0927-6505(01)00175-X
30. Aglietta M *et al*. (1996) A limit to the rate of ultra high energy ã-rays in the primary cosmic radiation, *Astroparticle Phys* **6** 71-75. doi: 10.1016/S0927-6505(96)00045-X
31. Chantell MC *et al*. (1997) Limits on the Isotropic Diffuse Flux of Ultrahigh Energy γ-Radiation. *Phys Rev Lett* **79** 1805-1808. http://dx.doi.org/10.1103/PhysRev

Lett.79.1805

32. Nonaka T *et al*. (2006) Did the 28 October 2003 solar flare accelerate protons to 20GeV A study of the subsequent Forbush decrease with the GRAPES-3 tracking muon telescope. *Phys Rev D* **74** 052003 1-15. doi: http://dx.doi.org/10.1103/PhysRevD.74.052003
33. Subramanian P *et al*. (2009) Forbush decreases and turbulence levels at coronal mass ejection fronts. *Astron Astrophys* **494** 1107-1118. doi: http://dx.doi.org/10.1051/0004-6361:200809551
34. Svestka Z (2001) Varieties of Coronal Mass Ejections and Their Relation to Flares. *Space Sci Rev* **95** 135-146. doi: 10.1023/A:1005225208925
35. Miller JA (1998) Particle Acceleration in Impulsive Solar Flares. *Space Sci Rev* **86** 79-105. doi: 10.1023/A:1005066209536
36. Reames DV *et al*. (1994) Energetic-Particle abundances in impulsive solar flare events. *Astrophys J Suppl* **90** 649-667
37. Reames DV (2000) Abundances of Trans-Iron Elements in Solar Energetic Particle Events *Astrophys J* **540** L111-L114
38. Reames DV and Ng CK (2004) Heavy-Element Abundances in Solar Energetic Particle Events. *Astrophys J* **610** 510-522
39. Wibberenz B *et al*. (1998) Transient Effects and Disturbed Conditions. *Space Sci Rev* **83** 309-348. doi: 10.1023/A:1005083109827
40. Fisk LA and Schwadron NA (2001) Origin of the Solar Wind: *Theory. Space Sci Rev* **97** 21-33.doi: 10.1023/A:1011805606787
41. Litvinenko YE (2002) Heavy Ion Abundances in Impulsive Solar Flares: Influence of Pre-Acceleration in a Current Sheet. *Solar Phys* **205** 341-349. doi: 10.1023/A:1014231124805
42. Litvinenko YE (2003) Particle Acceleration by a Time-Varying Electric Field in Merging Magnetic Fields. *Solar Phys* **216** 189-203. doi: 10.1023/A:1026143310271
43. Mandzhavidze N and Ramaty R (1993) Particle acceleration in solar flares. *Nucl Phys B Suppl* **33** 141-160. doi: 10.1016/0920-5632(93)90087-M
44. Kahler SW *et al*. (2001) Coronal Mass Ejections Associated with Impulsive Solar Energetic Particle Events. *Astrophys J* **562** 558-565
45. Miroshnichenko LI, Koning CAD and Perez-Enriquez R (2000) Large solar event of September 29, 1989: ten years after. *Space Sci Rev* **91** 615-715. doi: 10.1023/A:1005279108725
46. Aschwanden MJ (2002) Particle acceleration and kinematics in solar flares – A Synthesis of Recent Observations and Theoretical Concepts. *Space Sci Rev* **101** 1-227. doi: 10.1023/A:1019712124366
47. Charbonneau P *et al*. (2001) Avalanche models for solar flares. *Solar Phys* **203** 321-353. doi: 10.1023/A:1013301521745
48. Stone EC (1998) The Advanced Composition Explorer. *Space Sci Rev* **86** 1-22. doi: 10.1023/A:1005082526237
49. Karpov SN *et al*. (1997) Proc. 25th International Cosmic Ray Conference (MS Potgieter *et al*. Durban) 1 (1997) 205
50. Karpov SN, Miroshnichenko LI and Vashenyuk EV (1998) Muon bursts at the Baksan Underground Scintillation Telescope during energetic solar phenomena. *Nuovo Cimento C* **21** 551-575
51. Chiba N *et al*. (1992) Possible evidence for 10 GeV neutrons associated with the solar flare of 4 June 1991. *Astropart Phys* **1** 27. doi: 10.1016/0927-6505(92)90006-L
52. Ma Y *et al*. Proc. 28th International Cosmic Ray Conference (T Kajita *et al*. Tsukuba) 6 (2003) 3393
53. Forbush SE (1938) On World-Wide Changes in Cosmic-Ray Intensity. *Phys Rev* **54** (1938) 975-988. doi: http://dx.doi.org/10.1103/PhysRev.54.975
54. Lockwood JA (1971) Forbush decreases in the cosmic radiation. *Space Sci Rev* **12** 658-715. doi: 10.1007/BF00173346
55. Venkatesan D and Badruddin (1990) Cosmic-ray intensity variations in the 3-dimensional heliosphere. *Space Sci Rev* **52** 121-194. doi: 10.1007/BF00704241
56. Shea MA and Smart DF (1982) Possible evidence for a rigidity-dependent release of relativistic protons from the solar corona. *Space Sci Rev* **32** 251-271. doi: 10.1007/BF00225188
57. Cramp JL *et al*. (1997) The October 22, 1989, solar cosmic ray enhancement: An analysis of the anisotropy and spectral characteristics. *J Geophys Res* **102** 24237-24248. doi: 10.1029/97JA01947
58. Bieber JW (2005) Relativistic solar neutrons and protons on 28 October 2003. *Geophys Res Lett* **32** L03S02. doi: 10.1029/2004GL021492
59. Watanabe K *et al*. (2006) Solar Neutron Events of 2003 October November. *Astrophys J* **636** 1135-1144
60. Gupta SK *et al*. (2005) GRAPES-3—A high-density air shower array for studies on the structure in the cosmic-ray energy spectrum near the knee Nucl Instr Meth A 540 (2005) 311. doi: 10.1016/j.nima.2004.11.025
61. Hayashi Y *et al*. (2005) A large area muon tracking detector

for ultra-high energy cosmic ray astrophysics—the GRAPES-3 experiment *Nucl Instr Meth A* **545** (2005) 643-657. doi: 10.1016/j.nima.2005.02.020

62. Borione A *et al*. (1994) A large air shower array to search for astrophysical sources emitting ã-rays with energies ? 10^{14} eV, *Nucl Instr Meth A* **346** 329-352. doi: 10.1016/0168-9002(94)90722-6
63. Amenomori M *et al*. (1990) Development and performance test of a prototype air shower array for search for gamma ray point sources in the very high energy region. *Nucl Instr Meth A* **288** 619-631. doi: 10.1016/0168-9002(90)90161-X
64. Antoni T *et al*. (2001) Electron, muon, and hadron lateral distributions measured in air showers by the KASCADE experiment Astropart Phys 14: 245-260. doi: 10.1016/S0927-6505(00)00125-0
65. Antoni T *et al*. (2003) The cosmic-ray experiment KASCADE. *Nucl Instr Meth A* **513** 490-510. doi: 10.1016/S0168-9002(03)02076-X
66. Feenberg E and Primakoff H (1948) Interaction of Cosmic-Ray Primaries with Sunlight and Starlight. *Phys Rev* **73** 449-469. doi: http://dx.doi.org/10.1103/PhysRev.73.449
67. Hayakawa S (1952) Propagation of the Cosmic Radiation through Intersteller Space. *Prog Theor Phys* **8** 571-572. doi:10.1143/ptp/8.5.571
68. Morrison P (1958) On gamma-ray astronomy. *Nuovo Cimento* **7** 858-865. doi: 10.1007/BF02745590
69. Ong RA (1998) Very high-energy gamma-ray astronomy. *Phys Rep* **305** 93-202. doi: 10.1016/S0370-1573(98)00026-X
70. Hillas AM (1985) Proc of 19th Int Cosmic Ray Conf, *La Jolla* **3** 445
71. Gaisser TK *et al*. (1991) Gamma-ray astronomy above 50 TeV with muon-poor showers. *Phys Rev D* **43** 314-318. doi: http://dx.doi.org/10.1103/ PhysRevD.43.314
72. Mikocki S *et al*. (1991) Monte Carlo simulation of extensive air showers initiated by gamma rays and protons. *J Phys G: Nucl Part Phys* **17** 1303-1315. doi:10.1088/0954-3899/17/8/019
73. Cronin JW *et al*. (1992) Search for discrete sources of 100 TeV gamma radiation. *Phys Rev D* **45** 4385-4391. doi: http://dx.doi.org/10.1103/PhysRevD.45.4385
74. Aglietta M *et al*. (1995) Results on candidate UHE gamma-ray sources by the EAS-TOP array (1989-1993) *Astropart Phys* **3** 1-15. doi: 10.1016/0927-6505(94)00026-Y
75. Mohanty PK *et al*. (2009) Measurement of some EAS properties using new scintillator detectors developed for the GRAPES-3 experiment. *Astropart Phys* **31** 24-36. doi: 10.1016/j.astropartphys.2008.11.004
76. Oshima A *et al*. (2010) The angular resolution of the GRAPES-3 array from the shadows of the Moon and the Sun. *Astropart Phys* **33** 97-107. doi: 10.1016/j.astropartphys.2009.12.004
77. Greisen K (1960) Cosmic Ray Showers. *Ann Rev Nucl Sci* **10** 63-108. doi: 10.1146/annurev.ns.10.120160.000431
78. Kamata K and Nishimura J (1958) The Lateral and the Angular Structure Functions of Electron Showers. *Suppl Prog Theor Phys* **6** 93-155. doi: 10.1143/PTPS.6.93
79. Heck D *et al*. (1998) Report, FZKA 6019, Forschungszentrum Karlsruhe
80. Knapp J *et al*. (1996) Report, FZKA 5828, Forschungszentrum Karlsruhe
81. Heck D *et al*. (2001) Proc. 27th International Cosmic Ray Conference (Hamburg) **1** 233
82. Kalmykov NN, Ostapchenko SS and Pavlov AI (1997) Quark-gluon-string model and EAS simulation problems at ultra-high energies. *Nucl Phys B Proc Suppl* **52** 17-28. doi: 10.1016/S0920-5632(96)00846-8
83. Fletcher RS *et al*. (1994) SIBYLL: An event generator for simulation of high energy cosmic ray cascades. *Phys Rev D* **50** 5710-5731. doi: http://dx.doi.org/10.1103/PhysRevD.50.5710
84. Engel R *et al*. (1999) Proc. 26th International Cosmic Ray Conference (Salt Lake City) **1** 415
85. Drescher HJ, Hladik M, Ostapchenko S, Pierog T and Werner K (2001) Parton-based Gribov-Regge theory. *Physics Reports* **350** 93-289. doi: 10.1016/S0370-1573(00)00122-8
86. Fesefeldt H (1985) Report PITHA-85/02, RWTH Aachen
87. Bielajew AF *et al*. (1994) National Research Council Canada, NRC-PIRS-0436
88. Yoshikoshi T *et al*. (2001) Proc. 27th International Cosmic Ray Conference (Hamburg) **2** 612
89. Wiebel-Sooth B and Biermann Landolt-Bornstein P (1999) VI/3c Springer Verlag 37
90. Horandel JR (2003) On the knee in the energy spectrum of cosmic rays. *Astropart Phys* **19** 193-220. doi: 10.1016/S0927-6505(02)00198-6
91. Kasahara SM *et al*. (1997) Study of cosmic ray composition in the knee region using multiple muon events in the Soudan 2 detector. *Phys Rev D* **55** 5282-5294. doi: http://dx.doi.org/10.1103/PhysRevD.55.5282
92. Milke J *et al*. XXXIII Int Symp Multiparticle Dynamics, Krakow (2003)
93. Meli A and Biermann PL (2006) Cosmic rays X. The

cosmic ray knee and beyond: diffusive acceleration at oblique shocks. *Astron Astrophys* **454** 687-694. doi: http://dx.doi.org/10.1051/0004-6361:20064964

94. Ryan MJ *et al*. (1972) Cosmic-Ray Proton and Helium Spectra above 50 GeV. *Phys Rev Lett* **28** 985-988. doi: http://dx.doi.org/10.1103/PhysRevLett.28.985
95. Ivanenko IP *et al*. Proc. 23rd International Cosmic Ray Conference (Calgary) 2 (1993) 17
96. Grigorov NL *et al*. Proc. 12th International Cosmic Ray Conference (Hobart) 5 (1971) 1746
97. Lindner A *et al*. (1998) A new method to reconstruct the energy and determine the composition of cosmic rays from the measurement of Cherenkov light and particle densities in extensive air showers. *Astropart Phys* **8** (1998) 235-252. doi: 10.1016/S0927-6505(98)00004-8
98. Asakimori K *et al*. (1998) Cosmic-Ray Proton and Helium Spectra: Results from the JACEE Experiment. *Astrophys J* **502** 278-283
99. Apanasenko AV *et al*. (2001) Composition and energy spectra of cosmic-ray primaries in the energy range 10^{13}–10^{15} eV/particle observed by Japanese-Russian joint balloon experiment. *Astropart Phys* **16** 13-46. doi: 10.1016/S0927-6505(00)00163-8
100. Derbina VA *et al*. (2005) Cosmic-Ray Spectra and Composition in the Energy Range of 10–1000 TeV per Particle Obtained by the RUNJOB Experiment. *Astrophys J Lett* **628** L41-L44
101. Ahmed T *et al*. (1993) Total photoproduction cross section measurement at HERA energies. *Phys Lett B* **299** 374-384. doi: 10.1016/0370-2693(93)90277-O
102. Chekanov S *et al*. (2002) Measurement of the photon-proton total cross section at a center-of-mass energy of 209 GeV at HERA. *Nucl Phys B* **627** 3-28. doi: 10.1016/S0550-3213(02)00068-8
103. Chatelet E *et al*. (1990) Muons in EAS generated by cosmic gamma-rays with ultra-high energy. *J Phys G* **16** 317-325. doi:10.1088/0954-3899/16/2/019
104. Dingus BL *et al*. (1988) Search for signals from Cygnus X-3 at energies above 50 TeV. *Phys Rev Lett* **60** 1785-1788. http://dx.doi.org/10.1103/ PhysRevLett.60.1785
105. Dingus BL *et al*. (1988) Ultrahigh-Energy Pulsed Emission from Hercules X-1 with Anomalous Air-Shower Muon Production. *Phys Rev Lett* **61** 1906-1909. doi: http://dx.doi.org/10.1103/PhysRevLett.61.1906
106. Gupta SK *et al*. (1990) Episodic emission for Hercules X-1 at energies > 101^4eV. Astrophys J Lett **354** L13-L16
107. Suga K *et al*. (1963) Proc. 8th International Cosmic Ray Conference (Jaipur) 4: 9
108. Kamata K *et al*. (1968) Predominantly electromagnetic air showers of energy 10^{14} eV to 10^{16} eV. *Can J Phys* **46** S72-S74
109. Suga K *et al*. (1988) Diffuse gamma rays with energies greater than $1x10^{14}$ eV observed in the southern hemisphere. *Astrophys J* **326** 1036-1039
110. Gawin J *et al*. (1963) Proc. 8th International Cosmic Ray Conference (Jaipur) **4** 180
111. Gawin J *et al*. (1968) Remarks on mu-poor EAS. *Can J Phys* **46** S75-S77
112. Glushkov AV *et al*. (1985) Proc. 19th International Cosmic Ray Conference (La Jolla) **2** 186
113. Nikolsky SI, Stamenov JN and Ushev SZ (1987) Gamma quanta with energy ~ 10^{15} eV in the primary cosmic radiation. *J Phys G* **13** 883-895. doi:10.1088/0305-4616/13/6/014
114. Mathews J *et al*. (1991) Search for diffuse cosmic gamma rays above 200 TeV. *Astrophys J* **375** 202-208
115. Hayashi Y *et al*. (2003) Proc. 28th International Cosmic Ray Conference (Tsukuba) **4** 2273
116. Miroshnichenko LI *et al*. (2005) Relativistic nucleon and electron production in the 2003 October 28 solar event. *J Geophys Res* **110** A09S08-1-13. doi: 10.1029/2004JA010936
117. Miroshnichenko LI (2003) Proc. 28th International Cosmic Ray Conference (Tsukuba) **6** 3321
118. Cane HV (2000) Coronal Mass Ejections and Forbush Decreases. *Space Sci Rev* **93** 55- 77. doi: 10.1023/A:1026532125747.